Forschungszentrum Karlsruhe
in der Helmholtz-Gemeinschaft

Wissenschaftliche Berichte

FZKA 6794

Verification of a fracture mechanics concept for the cleavage fracture behaviour of RAFM steels using local fracture criteria

Final Report for Task TW2-TTMS-005/D3

H. Riesch-Oppermann

Institut für Materialforschung
Programm Kernfusion
Association Forschungszentrum Karlsruhe / EURATOM

Forschungszentrum Karlsruhe GmbH, Karlsruhe

2003

Impressum der Print-Ausgabe:

Als Manuskript gedruckt

Forschungszentrum Karlsruhe GmbH
Postfach 3640, 76021 Karlsruhe

Mitglied der Hermann von Helmholtz-Gemeinschaft
Deutscher Forschungszentren (HGF)

ISSN 0947-8620

Abstract

An effort is made within the European Fusion Technology Programme framework to obtain a fracture mechanics description of the material behaviour in the ductile to brittle transition-regime using local fracture criteria. In a companion report, the necessary procedural steps towards the development of an according design code scheme were described. The present report contains application examples and verification results of the different procedural steps and identifies limitations of the approach for the two reference RAFM steels F82Hmod and EUROFER97.

Zusammenfassung

Verifikationsschritte für eine bruchmechanische Beschreibung des Sprödbruchverhaltens niedrigaktivierbarer Stähle auf Basis lokaler Versagenskriterien

Innerhalb des Europäischen Fusionsprogramms wird eine bruchmechanische Beschreibung des Materialverhaltens im Bereich des spröd-duktilen Übergangs auf Basis lokaler Versagenskriterien angestrebt. In einem separaten Bericht wurden die dazu notwendigen Schritte für die Entwicklung eines entsprechenden Designcodes beschrieben. Der vorliegende Bericht enthält Beispiele zu deren Anwendung und Verifizierung auf Basis von Ergebnissen für die beiden Stahlsorten F82Hmod und EUROFER 97. Dabei werden auch die Grenzen des betrachteten Ansatzes aufgezeigt.

Contents

1 General **1**

1.1 Scope 1

1.2 Organisation of the report 1

1.3 Related documents 2

2 Material deformation characteristics **2**

3 Finite Element Analysis **3**

4 Experimental cleavage fracture data base **3**

5 Weibull stress calculation **4**

5.1 Stress analysis of fractured specimens 4

5.2 Stress envelope extraction 4

5.3 Calculation of the Weibull stress 4

6 Fractographic analysis **5**

6.1 Fracture appearance 5

6.2 Fracture origin distribution 6

6.3 Numerical analysis & fractographic results 6

6.4 Additional experimental evidence on fracture mechanisms 6

7 Statistical inference results **7**

7.1 Maximum likelihood estimation 7

7.2 ML confidence intervals 7

7.3 Bootstrap confidence intervals 7

8 Use of local risk of rupture for transferability assessment **8**

8.1 Notched specimen results 8

8.2 Pre-cracked specimen results 9

9 Limitations of the cleavage fracture model with respect to RAFM steels 9

10 Summary and conclusions 10

A Figures 13

B Tables 39

List of Figures

1 F82Hmod Charpy V results in as-received condition. 13
2 F82Hmod true stress-strain curves 14
3 EUROFER97 true stress-strain curves 14
4 Hardening behaviour 15
5 F82Hmod force-elongation curves 15
6 Axial stress distribution (F82Hmod, 2mm) 16
7 Triaxiality ratio (F82Hmod, 2mm) 17
8 Axial stress distribution (EUROFER97, 0.5mm) 18
9 Triaxiality ratio (EUROFER97, 0.5mm) 19
10 Axial stress distribution (EUROFER97, 2mm) 20
11 Triaxiality ratio (EUROFER97, 2mm) 21
12 Triaxiality ratio (F82Hmod, 2mm) along symmetry line 22
13 Triaxiality ratio (EUROFER97, 2mm) along symmetry line 23
14 Geometry of axisymmetrically notched bar (RNB) specimens. 24
15 F82Hmod: fracture stress and strain at -150° C 24
16 F82Hmod: fracture stress and strain at -75° C 25
17 FE stress analysis and fracture loci (F82Hmod, -150° C) 25
18 FE stress analysis and fracture loci (F82Hmod, -75° C) 26
19 FE stress analysis and fracture loci (EUROFER97, -150° C) 26
20 Flow diagram for iterative Weibull parameter estimation procedure. . 27
21 Weibull stress calculation (F82Hmod, -150° C) 27
22 Weibull stress calculation (F82Hmod, -75° C) 28
23 Weibull stress calculation (EUROFER97, -150° C) 28
24 SEM section of F82Hmod in reference condition. 29
25 Fracture origin (F82Hmod, 2mm, -150° C) 29
26 Fracture surface (F82Hmod, 2mm, -75° C) 30
27 Fracture surface (F82Hmod, 5mm, -150° C) 30

28 Stress distribution and fracture origins (F82Hmod, 1mm, -150° C) . . 31
29 Stress distribution and fracture origins (F82Hmod, 2mm, -75° C) . . . 31
30 Fracture origin locations (F82Hmod, 1+2mm, -150° C) 32
31 Strain induced lath reorientation 33
32 Bootstrap confidence intervals 34
33 Bootstrap confidence intervals 34
34 Scatterplot of bootstrap results (F82Hmod, 1mm, -150° C) 35
35 Scatterplot of bootstrap results (F82Hmod, 2mm, -150° C) 35
36 Fracture origin distribution (F82Hmod, 1mm, -150° C) 36
37 Fracture origin distribution (F82Hmod, 2mm, -150° C) 36
38 Fracture origin distribution (EUROFER97, 0.5mm, -150° C) 37
39 Fracture origin distribution (EUROFER97, 2mm, -150° C) 37
40 Risk of rupture (F82Hmod, pre-cracked, -150° C) 38

List of Tables

1 Composition (wt-%) of F82Hmod; Heat No. 9741 39

2 Composition (wt-%) of EUROFER 97; Heat No. E83689 39

3 F82Hmod material parameters 40

4 EUROFER97 material parameters 40

5 F82Hmod 1mm notched specimens 41

6 Part of the auxiliary `*.wst`-file. 42

7 Part of the Weibull stress results file. 43

7 (cont'd.) 44

7 (cont'd.) 45

7 (cont'd.) 46

8 Maximum likelihood results (F82Hmod) 47

9 Maximum likelihood results (EUROFER97) 47

10 Unbiasing factors $b(N)$ 48

11 Auxiliary variables for the confidence interval for σ_u 49

11 Auxiliary variables for the confidence interval for σ_u (cont'd.) 50

12 Auxiliary variables for the confidence interval for m 51

12 Auxiliary variables for the confidence interval for m (cont'd) 52

13 Comparison of confidence intervals (F82Hmod) 53

14 Comparison of confidence intervals (EUROFER97) 53

1 General

The present analysis is part of the **EURATOM Fusion Technology - Blanket** programme for 1999 to 2002 under EFDA Reference TW2-TTMS-005 **Structural Materials: Rules for Design, Fabrication, and Inspection**.

1.1 Scope

In the companion report [12], the procedural steps for a local approach to cleavage fracture were described as an alternative approach to a basic route of structural integrity assessment.

In the present report, the procedural steps are described in detail and on the basis of experimental results for the two RAFM steel variants F82Hmod and EUROFER97.

1.2 Organisation of the report

The contents are organized as to follow the subsequent steps of the analysis:

Section 2 contains information about the material properties relevant for the stress analysis of the used specimens and how they are obtained.

Section 3 contains results of calculations used to obtain suitable specimen geometries for the axisymmetrically notched tensile bars.

Section 4 contains results of the cleavage fracture experiments that are basis for the Weibull stress calculation.

Section 5 contains the Weibull stress calculation procedure and results. Statistical inference results are described in Section 7.

In Section 6, selected fractographic results are presented and compared to results of the Weibull parameter results in Section 5 and Section 7, respectively.

Section 8 describes how the local risk of rupture can be used to assess transferability between different specimen geometries.

Section 9 describes the material-specific limitations of the cleavage fracture model that could be identified from a combined analysis of the numerical and fractographic results.

Section 10 summarizes the results and contains remarks on possible future topics of interest.

For the definitions of terms and details about the procedural steps used in this document, see [12].

All figures are contained in Appendix A. Appendix B contains the necessary tables.

1.3 Related documents

Evaluation of cleavage fracture parameters is currently under standardization efforts in different contexts (SINTAP [9], R6 [2], ESIS [6], ASTM [5]). Part of the procedures described in this document were tested and verified within an ESIS round robin [10].

The procedural steps used in this report are fully described in a companion report [12] which also contains the definitions of terms used in this document.

2 Material deformation characteristics

Chemical composition of the material is shown in Tables 1 (F82Hmod, heat No. 9741 [7]) and 2 (EUROFER97, heat No. E83689 [7]). Ductile-to-brittle transition behaviour in Charpy tests [15] for F82Hmod is shown in Figure 1. Material characteristics for the elasto-plastic deformation behaviour were obtained from smooth tensile bar tests at relevant temperature [17]. The tests were conducted at -150° C, -75° C and ambient temperature (25° C). Figures 2 (F82Hmod) and 3 (EUROFER97) show results of true stress-strain curves up to necking obtained from load-vs-displacement records. Figure 4 shows the hardening behaviour of the two materials. Young's modulus E and true stress-strain curves were obtained from load F vs. extensometer longitudinal displacement l measurements (see Fig. 5) up to necking of the specimens. True stresses σ and strains ε were calculated from engineering stresses $s = F/A_0$ and strains $e = \Delta l/l_0$ according to the relations:

$$\varepsilon = \ln(1+e) \qquad \text{and} \qquad \sigma = s(1+e). \tag{1}$$

Eqns. (1) are based on the presence of a homogeneous strain distribution along the gage length and a constant volume relationship and thus are valid only to the onset of necking of the specimen [4]. An elastic-plastic material law with a hardening exponent of n and temperature dependent 0.2% offset yield strength σ_0 was fitted to the true plastic strain range of $[.1\%,\ldots,10\%]$ according to the so-called Ludwik [8] or Hollomon relation

$$\sigma = K\varepsilon_{\mathrm{pl}}^{n}. \tag{2}$$

A summary of the parameters that are used for the subsequent analysis of the axisymmetrically notched tensile specimens is given in Table 3 (for F82Hmod) and in Table 4 (for EUROFER97). Young's modulus, E, is determined from the load-displacement recordings of the extensometer displacement values before necking. Figure 4 shows the resulting hardening properties for F82Hmod and EUROFER97, respectively. Yield stress is somewhat larger and the hardening is more pronounced for F82Hmod compared to EUROFER97 as indicated by the somewhat smaller value of the hardening exponent, n, for F82Hmod in Eq. 2.

3 Finite Element Analysis

The general purpose Finite Element code ABAQUS was used for the analysis [1]. A piecewise linear stress-strain law is used in the Finite Element analysis of the notched bar specimen geometries. Beyond necking strain, extrapolation of the stress-strain law was done using Eq. 2.

As a result of the analysis, the axial stress distribution along the minimum diameter was obtained as well as the triaxiality ratio along the minimum diameter. While the basic geometry of the specimens remained fixed, notch radii of 1, 2, and 5mm were investigated for F82Hmod (see [14]). Figures 6 and 7 show some results for the axial stress distribution and the triaxiality ratio obtained for F82Hmod. Stresses and triaxiality ratios are shown along a radial line starting at the notch root and ending at the specimen axis.

For EUROFER97, additional notch radii of 0.5mm and 4mm were selected for the analysis. Figures 8 and 9 show the axial stress distribution and the triaxiality ratio at the three temperature levels for a notch radius of 0.5mm. In Figures 10 and 11, the corresponding results for a notch radius of 2mm are shown.

Figures 12 and 13 show triaxiality ratios along the symmetry line of the specimen indicating that displacement boundary conditions are not affected by presence of notch stress concentrations and the stress state at the boundary is uniaxial.

Each of the Figures in this Section is composed of four parts which show results at -150° C (upper left), at -75° C (upper right), and at +25° C (lower left) together with the mesh geometry (lower right) used for the analysis.

4 Experimental cleavage fracture data base

Axisymmetrically notched tensile specimens are used for cleavage fracture characterization. The specimen geometry is shown in Figure 14.

As a result of the tensile tests on axisymmetrically notched specimens, a sample of fracture loads together with the corresponding diametral contractions at fracture is obtained for each temperature and each notch radius.

Continuous recording of load and diametral contraction is used for subsequent verification of the Finite Element stress analysis of fractured specimens.

Figure 15 shows mean stress and strain values at fracture for F82Hmod sprecimens with different notch radii tested at -150 ° C. Figure 16 shows the corresponding results for a test temperature of -75 ° C.

Table 5 contains reporting of results for r=1mm notched F82Hmod specimens tested at -150 ° C. For each specimen tested, corresponding values of diameter reduction Δd,

fracture load F, mean strain ε_M and mean stress σ_M at fracture are listed. The last column contains the corresponding Weibull stress values σ_W (see Section 5).

5 Weibull stress calculation

Weibull stress calculation requires two preparatory steps. In a first step, the stress field at fracture in each specimen of a sample is calculated. In the second step, the maximum value of the first principal stress until fracture is extracted for each location within the specimen. This is done to account for stress redistribution effects that may lead to locally decreasing first principal stress values with increasing loading. The resulting values of the first principal stresses at fracture are termed the stress envelope. The Weibull stress is then calculated using the stress envelope. A symmetry factor of $sym = 2 * 2\pi\text{rad} = 12.57$ is applied due to the axisymmetric modelling of half of the specimen geometry.

5.1 Stress analysis of fractured specimens

Results of the FE stress analysis together with the experimentally observed fracture loci for F82Hmod at -150° C are shown in Figure 17. Figure 18 shows the results for a test temperature of -75° C. The results for EUROFER97 are shown in Figure 19.

5.2 Stress envelope extraction

The `WEISTRABA` FE-Postprocessor [13] is used to extract the envelope of first principal stresses at fracture. For the subsequent calculation of the Weibull stress, an auxiliary (`*.wst`-) file is generated containing all of the necessary information of the FE stress analysis, i.e. nodal coordinates, element list, nodal stress envelope values, plastic zone flags. A part of the auxiliary `*.wst`-file is shown in Table 6. Comments indicate the meaning of the data columns.

5.3 Calculation of the Weibull stress

For the calculation of the Weibull stress, the Weibull parameter m has to be known. The Weibull parameters are determinated using an iterative procedure as described in [12] and sketched in Figure 20. Starting with an initial value of $m = 20$ for the Weibull modulus, convergence is typically achieved after 2-5 steps. Table 7 shows part of the results file. The summary at the end of the file contains the final Weibull stress values for each load step (see also Table 5), the final values of the Weibull parameters

m and σ_u and the confidence intervals for both Weibull parameters at three different confidence levels.

Detailed results for the Weibull parameters are given in Section 7.

The results show that for F82Hmod, two groups of results can be identified. In the first group, moderate values of m are present (see Figure 21), while for the second group, m attains high values of about 80-100 (see Figure 22),.

For EUROFER97, results for 0.5mm notched tensile specimens fall into the first group, whereas the 2mm notched specimens seem to belong to the second group (see Figure 23).

The two groups are characterized by pronounced differences in the mean strain at fracture. While the mean strain at fracture, ε_M, is less than about 10% for the first group, it attains values exceeding 50% for the second group. The reason for these differences lies in the fracture process which is different for the two groups and which can be identified and explained by fractographic analysis.

6 Fractographic analysis

Results of fractographic analyses are given exemplarily for F82Hmod experiments. The microstructure of F82Hmod steel is fully martensitic and free of δ-ferrite. Due to the small carbon content, lath martensite is prevalent. Between the martensite laths and along the former austenite grain boundaries, $(\mathrm{Fe,Cr,W})_{23}\mathrm{C}_6$ precipitations are present. Apart from the carbide precipitations, oxide particles are also present, mainly in the form of $(\mathrm{Ti,Ta})_{1-x}\mathrm{O}_x - \mathrm{Al}_2\mathrm{O}_3$. Figure 24 shows an example of an SEM section of F82Hmod in reference condition.

6.1 Fracture appearance

For the first (small fracture strain) group, corresponding to low temperature and small notch radii, fractography showed pure cleavage fracture. Fracture origins could be easily detected as shown in Figure 25. Cleavage fracture started from $(\mathrm{Ti,Ta})_{1-x}\mathrm{O}_x - \mathrm{Al}_2\mathrm{O}_3$ Oxide inclusions which could be identified by SEM at nearly all of the fracture initiation sites.

Figures 26 and 27 show two fracture surfaces of specimens tested at -75° C (2mm notch radius) and -150° C (5mm notch radius) which both belong to the second (large fracture strain) group. A mixed trans- and intercrystalline appearance can be observed with indications of ductile damage at the temperature level of -75° C. Fracture origin locations could be identified for nearly all specimens but no inclusions or other fracture initiating particles were present [17].

6.2 Fracture origin distribution

From the fracture origin location identification it was possible to relate fracture origin sites and stress field at fracture [17]. Fig. 28 shows results of the stress analysis together with the fracture origins from the fractographic analysis for $r = 1$mm notched F82Hmod specimens tested at $T = -150^\circ$C. The location of the fracture origins is evenly distributed along the specimen diameter and is not correlated with the value of the axial stresses hat are responsible for fracture. This reflects the fact that a combination of stress field and microcrack size together is relevant for the fracture process.

For the specimens in the second (large fracture strains) group, Fig. 29 shows a typical result for the stress analysis together with the fracture origins from fractographic investigations. Here, the location of the fracture origins is concentrated in the vicinity of the specimen axis.

The fracture origin distribution for 1 and 2mm notched specimens tested at $T = -150^\circ$C is shown in Fig. 30. While the fracture origins are evenly distributed along the specimen diameter for the $r = 1$mm notched F82Hmod specimens (see Fig. 28), they tend to lie closer to the specimen axis for the $r = 2$mm notched specimens. Section 8 will give a numerical analysis using the local risk of rupture for these two cases.

6.3 Numerical analysis & fractographic results

Fractography gives a consistent interpretation of the experimental findings evaluated by numerical Weibull stress analysis. Differences in value and scatter correspond to different fracture initiation mechanisms. Contrary to pure ferritic (e.g. RPV) steels such as 20 MnMoNi 5 5 or its variants, the microstructural martensitic features play a dominant role in the fracture initiation process. This can be seen from the presence of axial cracks at specimens with a large notch radius or tested at higher temperatures, both of which exhibit large fracture strains.

6.4 Additional experimental evidence on fracture mechanisms

The origin of the axial cracks is presumably due to the reorientation of the martensite laths at locations where large plastic strains are present. In the sequel, debonding of the second phase particles which are located preferentially at the lath boundaries as well as the former austenite grain boundaries occurs and leads to shear-controlled initiation of cracks which are oriented in axial direction. This can be seen from additional experiments on flat notched specimens at room temperature, where reorientation of the martensite laths could be observed [11]. In Figure 31, two SEM micrographs are shown. The first (top) shows the orientation of martensite laths in an undeformed part of the specimen at remote notch distance, where no preferential orientation is present.

The second micrograph (bottom) shows the orientation of martensite laths in the vicinity of the notch, where the preferential martensite lath orientation in axial direction is clearly visible.

7 Statistical inference results

Statistical inference for the cleavage fracture parameters is done using the iterative maximum likelihood procedure as described in [12]. In a second step, confidence intervals are obtained. As the maximum likelihood confidence intervals are not strictly valid for the iterative Weibull parameter estimation procedure, results of an alternative approach; the so-called resampling (or bootstrap) method, are presented as well.

7.1 Maximum likelihood estimation for m and σ_u

Maximum likelihood estimates are obtained according to Figure 20. Tables 8 for F82Hmod and 9 for EUROFER97 contain results for the Weibull parameters. Weibull plots of the resulting Weibull stress values are shown in Figures 21 and 22 for F82Hmod and in Figure 23 for EUROFER97.

Unbiasing factors for the calculation of the unbiased estimate $\hat{m}_{unb}$ for the Weibull modulus m are given in Table 10.

7.2 Confidence intervals for m and σ_u based on maximum likelihood estimators

Maximum likelihood confidence intervals for m and σ_u are determined using Tables 10, 11 and 12 which were taken from Ref. [16] and are also contained in [3]. It should be noted, that the confidence intervals obtained in this way are not strictly valid for the iterative Weibull parameter estimation procedure.

7.3 Confidence intervals for m and σ_u based on resampling methods

Figure 32 shows schematically how bootstrap confidence intervals are obtained using the empirical cumulative distribution of bootstrap replication results. The left curve is the standard normal distribution function which is used for the determination of the bias correction factor as indicated by the arrows. A value of $z_0^m = -0.29$ indicates considerable bias towards higher values of $\hat{m}$ leading to a compensating downward shift of the confidence bounds.

In Figure 33, where the bias is not so pronounced, but a heavy tail at high m-values is present, the different confidence intervals are indicated by horizontal lines. In this case, the ordinary maximum likelihood based confidence intervals lead to a considerable shift of the confidence limits to lower m-values whereas the bootstrap intervals are sensitive to the heavy tail of the m-distribution.

Comparison of the confidence intervals using ML and bootstrap method is shown in Tables 13 and 14, respectively. Figures 34 and 35, respectively show results of bootstrap replications for $(\hat{m}, \widehat{\sigma_u})$-pairs obtained from a series of $B = 200$ bootstrap simulations. A strong correlation is apparent in both cases. Results of 2mm notched specimens additionally exhibit a pronounced grouping of the results indicating that one or more of the data points are suspicious and presumably do not belong to the same population as the rest, i.e. homogeneity of the data set may be violated. Both, correlation as well as data inhomogeneities are not addressed with ordinary maximum likelihood based confidence intervals and only visible as result of bootstrap simulations. Values of the confidence limits themselves are difficult to compare qualitatively due to the limited number of specimens leading to comparatively large scatter especially in the values for $\hat{m}$.

8 Use of local risk of rupture for transferability assessment

The local risk of rupture [11] is obtained as conditional probability of having a microcrack in some sub-volume, V_s, of the specimen under the condition that this microcrack causes unstable fracture at the current load level characterized by the value of the Weibull stress, σ_W. Integration over the whole range of σ_W-values leads to the integrated local risk of rupture which corresponds to the fracture origin location distribution. Comparison of the fracture origin location distribution obtained from integration of the local risk of rupture with the fracture origin location distribution obtained from fractographic analysis is used for the assessment of the applicability of cleavage fracture models.

8.1 Notched specimen results

Figures 36 and 37 show the fracture origin location distribution obtained from the integrated local risk of rupture values for F82Hmod 1mm and 2mm notched specimens tested at -150 °C. The corresponding results obtained from fractographic analysis of the fractured specimens are shown in Figure 30. The calculated and experimentally observed fracture origin distribution turn out to be in qualitative agreement.

Figures 38 and 39 show the fracture origin location distribution obtained from the integrated local risk of rupture values for EUROFER97 0.5mm and 2mm notched specimens tested at -150 °C. For the 2mm notched specimen, the fracture origin location distribution is concentrated at a small volume in the specimen centre, while for the 0.5mm notched specimen, the most probable fracture initiation sites have a wide distribution around the midpoint between specimen centre and notch root. In that case, a large number of weak spots can be sampled, whereas in the former case only a very small volume is available.

Unfortunately, no corresponding fractographic results are yet available to confirm this findings for EUROFER97.

8.2 Pre-cracked specimen results

A limited number of axisymmetrically pre-cracked specimens was tested [14, 17] and analysed giving Weibull stress values and local risk of rupture data. Figure 40 shows the calculated risk of rupture density for deeply pre-cracked specimens at a load level corresponding to the highest fracture strain for deeply pre-cracked specimens. It can be seen that the predicted local risk of rupture is confined to a small region close to the crack tip ($\leq 40\mu m$, which is about the distance from crack tip to the left image border of Figure 40). Fractography, however, revealed that the fracture origins were located in the vicinity of the crack front at a distance of about 150-400 μm. Unlike for the notched specimens, no cleavage fracture facets were observed and oxide inclusions were found at only about 40% of the fracture origin sites [14].

9 Limitations of the cleavage fracture model with respect to RAFM steels

The present results for F82Hmod and EUROFER97 RAFM steels show a limited applicability of local approach methodology as recommended in the ESIS P6 [6] procedure. The limitations are due to a fracture initiation process that is different from ordinary ferritic steels. Due to the presence of carbide decorated grain boundaries and martensite laths, strain induced formation of microcracks in axial direction is promoted in case of large fracture strains leading to a mixed trans/intergranular fracture appearance. Large fracture strains can be caused by elevated temperature levels and/or lower degrees of triaxiality. Transferability is therefore only possible if presence of identical fracture mechanisms can be justified by fractographic investigations.

10 Summary and conclusions

The present report contains results of cleavage fracture characterization for F82Hmod and EUROFER97 RAFM steels using local approach methodology that is well established for ordinary (RPV) ferritic steels. The numerical procedure for the determination of cleavage fracture parameters is well established while the statistical characterization of the parameters is subject to ongoing work.

The objective of the task was to develop fracture mechanics rules for RAFM steels on the basis of the ”local approach” and to transfer experience gained with F82Hmod results to EUROFER97. In a later stage, results should be incorporated into a framework for modelling irradiation effects.

A set of design curves should be generated wherefrom critical cleavage fracture parameters could be obtained without the need of extensive Finite Element analysis and validation support should be obtained by use of the local risk of rupture.

The results obtained can de summarized as follows: Fracture mechanics rules based on the ”local approach” are summarized in the companion report [12]. The numerical procedures are available and partly verified within Round Robin activities [10]. Methods of statistical inference were developed and allow improved analysis of cleavage fracture data with respect to homogeneity and correlation structure compared to methods used in present codes like [6, 2]. However, due to the pronounced influence of the martensitic microstructure on the cleavage fracture process a straightforward extension of the methodology was not possible.

While a detailed analysis of the cleavage fracture behaviour could be obtained, different fracture mechanisms required an individual analysis of the experimental results obtained at different temperature levels. Generation of a set of material curves for design purposes was therefore not possible because of limitations in the applicability of the approach.

The additional fracture mode of a mixed trans-/intergranular fracture appearance characterized by the presence of axial cracks leads to a separation of the cleavage fracture results in two groups. Transferability of the results is only possible within one group but not between groups.

It should be emphasized that most of the conclusions on cleavage fracture behaviour could be derived from numerical results and the corresponding statistical inference methods but had to be confirmed by fractographic analysis.

Acknowledgement

This report covers work performed in the framework of the Nuclear Fusion Programme of the Forschungszentrum Karlsruhe.

Support of the European Community via the 5th framework Fusion Technology Programme under task ID TTMS-005 is gratefully acknowledged.

Part of the numerical methods have been developed within the context of a center of collaborative research at Karlsruhe University (SFB483) for which financial support of the Deutsche Forschungsgemeinschaft is appreciated.

References

[1] ABAQUS/Standard User's Manual (Version 5.8), Hibbit, Karlsson & Sorensen, Inc. 1998.

[2] British Energy Generation Ltd., Assessment of the integrity of structures containing defects - Revision 4, 2001.

[3] European Standard ENV 843-5, Advanced monolithic ceramics - mechanical tests at room temperature - statistical analysis.

[4] G.E. Dieter, Mechanical Metallurgy, McGraw-Hill Book Company, London, 1988.

[5] E 1921 - 97, Standard Test Method for Determination of Reference Temperature, T_0, for Ferritic Steels in the Transition Range, ASTM, Annual Book of ASTM Standards, Vol 03.01., 2001, 1119-1135.

[6] ESIS P6 - 98, Procedure to Measure and Calculate Local Approach Criteria Using Notched Tensile Specimens, ESIS Document, European Structural Integrity Society, March 1998.

[7] R. Lindau, Forschungszentrum Karlsruhe, Personal communication.

[8] P. Ludwik, Elemente der technologischen Mechanik, Springer, 1909.

[9] H.G. Pisarski, K. Wallin, The SINTAP fracture toughness estimation procedure, Engineering Fracture Mechanics **67** (2000), 613-624.

[10] H. Riesch-Oppermann, FZK Contribution to the ESIS TC 8 Numerical Round Robin on Micromechanical Models (Phase II, Task B1), FZKA Report 6338, Forschungszentrum Karlsruhe, 1999.

[11] H. Riesch-Oppermann, E. Diegele, Towards a micro-mechanical description of the fracture behaviour for RAFM steels in the ductile-to-brittle transition regime, J. Nucl. Materials **307-311** (2002), 1021-1025.

[12] H. Riesch-Oppermann, E. Diegele, Elements of a fracture mechanics concept for the cleavage fracture behaviour of RAFM steels using local fracture criteria, FZKA Report 6668, Forschungszentrum Karlsruhe, 2002.

[13] H. Riesch-Oppermann, A. Brückner-Foit, WEISTRABA - A code for the numerical analysis of Weibull stress parameters from ABAQUS finite element stress analyses - Procedural background and code description -, FZKA Report 6155, Forschungszentrum Karlsruhe, August 1998.

[14] H. Riesch-Oppermann, M. Walter, Status report on experiments and modelling of the cleavage fracture behaviour of F82Hmod using local fracture criteria: Task TTMS-005 , Report FZKA 6388, Forschungszentrum Karlsruhe, 2001.

[15] M. Rieth, Forschungszentrum Karlsruhe, personal communication.

[16] D.R. Thoman, L.J. Bain, C.E. Antle, Inferences on the Parameters of the Weibull Distribution, Technometrics, **11** (1969), 445-460.

[17] M. Walter, Mechanische und fraktographische Charakterisierung des niedrigaktivierbaren Chromstahls F82H-mod im spröd-duktilen Übergangsbereich, Dissertation, Report FZKA 6657, Forschungszentrum Karlsruhe, 2002.

A Figures

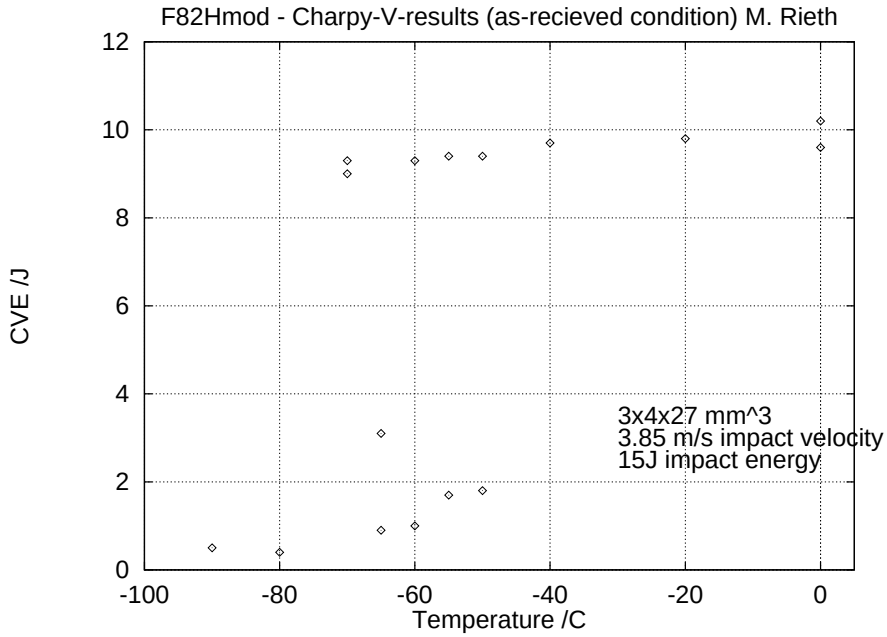

Figure 1: F82Hmod Charpy V results in as-received condition.

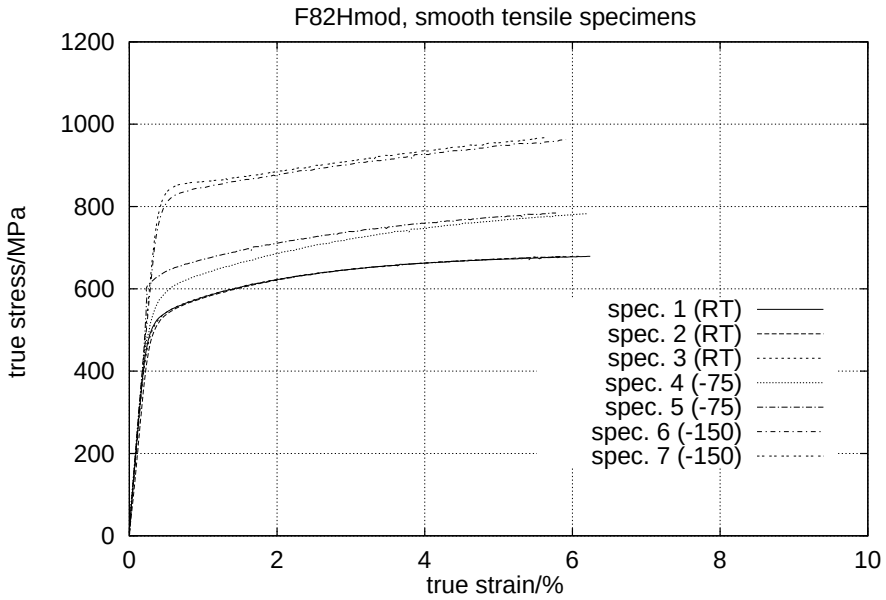

Figure 2: Results of true stress-strain curves up to necking obtained from load-vs-displacement records for F82Hmod.

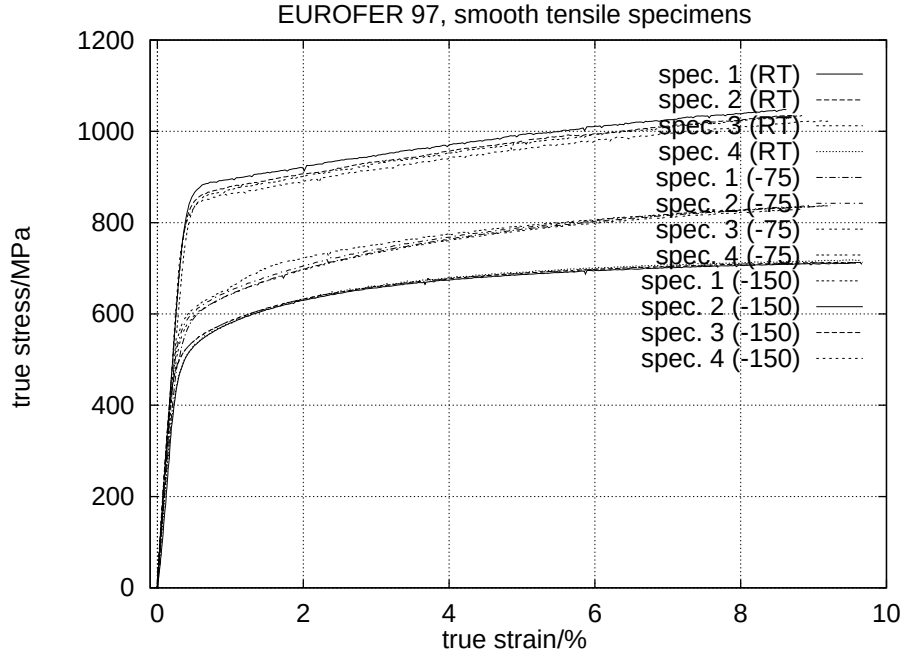

Figure 3: Results of true stress-strain curves up to necking obtained from load-vs-displacement records for EUROFER97.

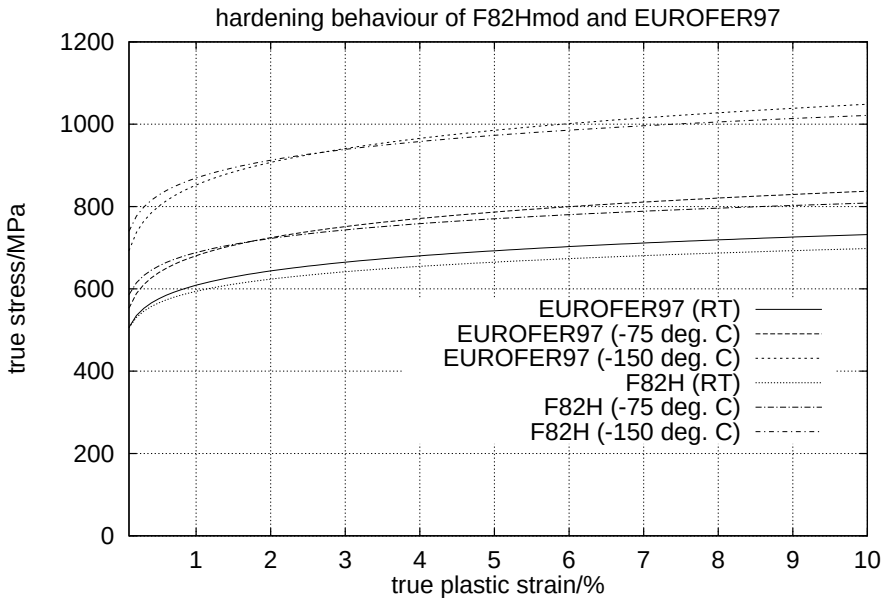

Figure 4: Hardening behaviour of the two RAFM steels F82Hmod and EUROFER97, respectively.

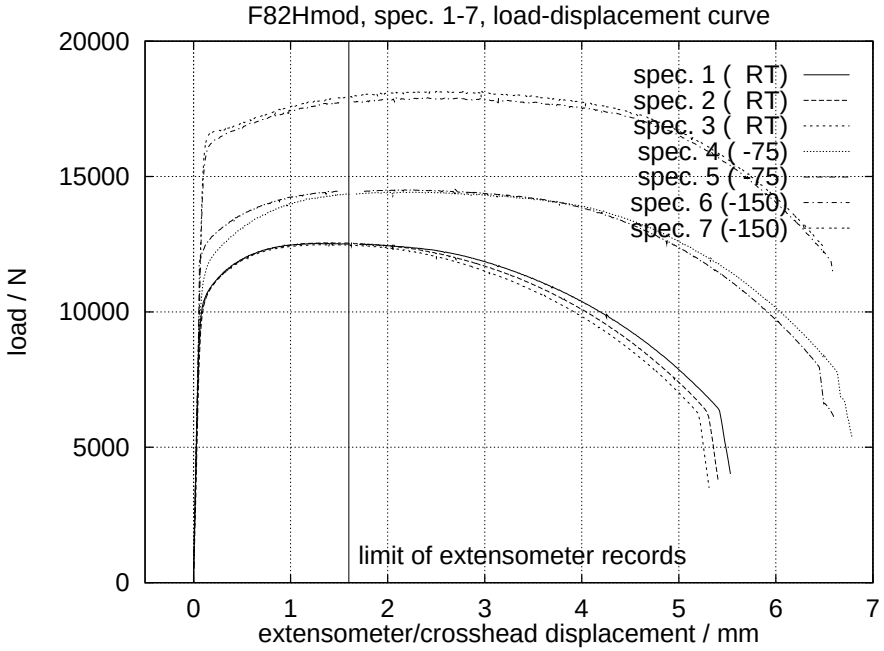

Figure 5: Results of load-vs-displacement recording for F82Hmod at different temperatures. Only extensometer-based results were used for the determination of material behaviour.

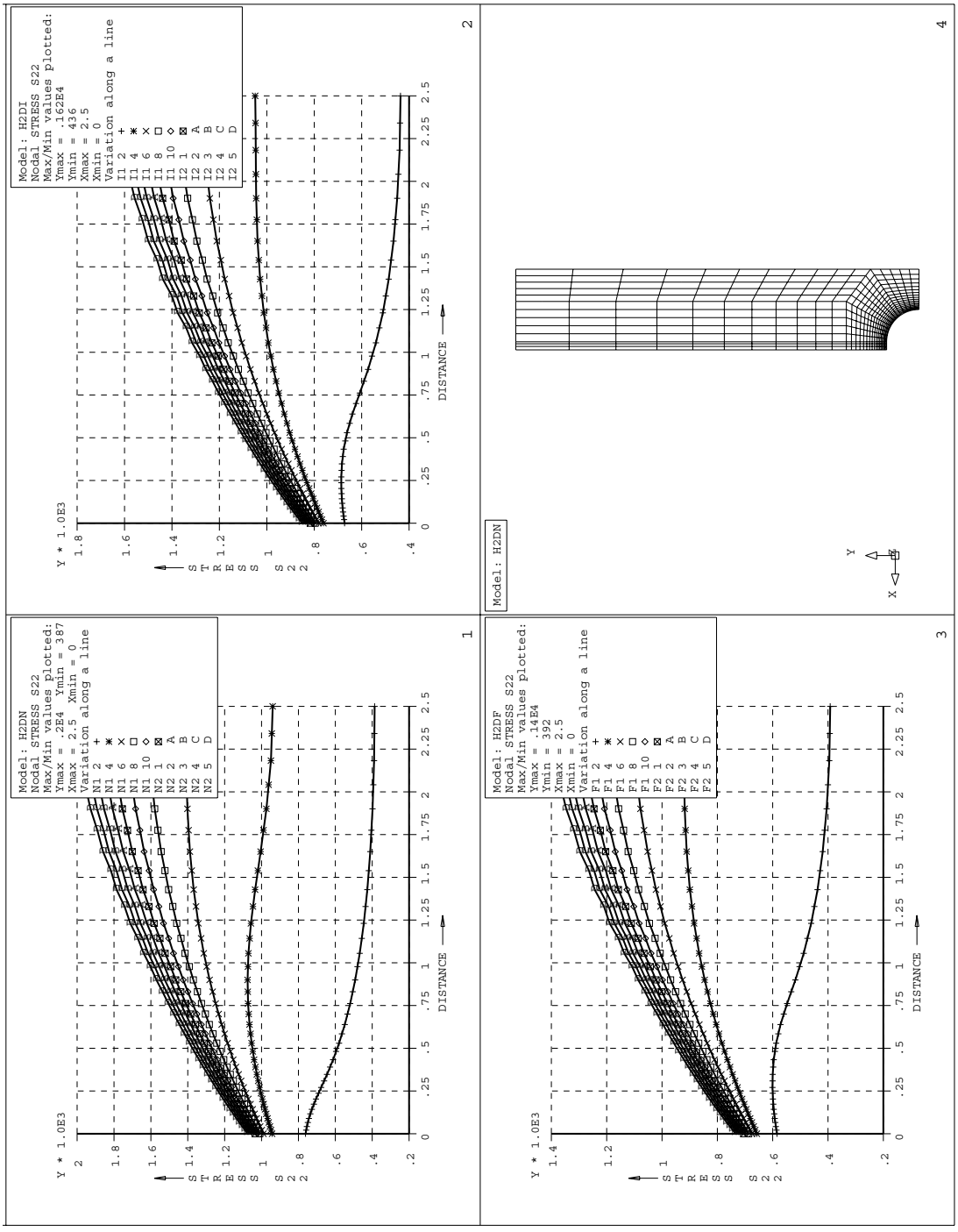

Figure 6: Axial stress distribution (F82Hmod) at three temperature levels for a notch radius of 2mm.

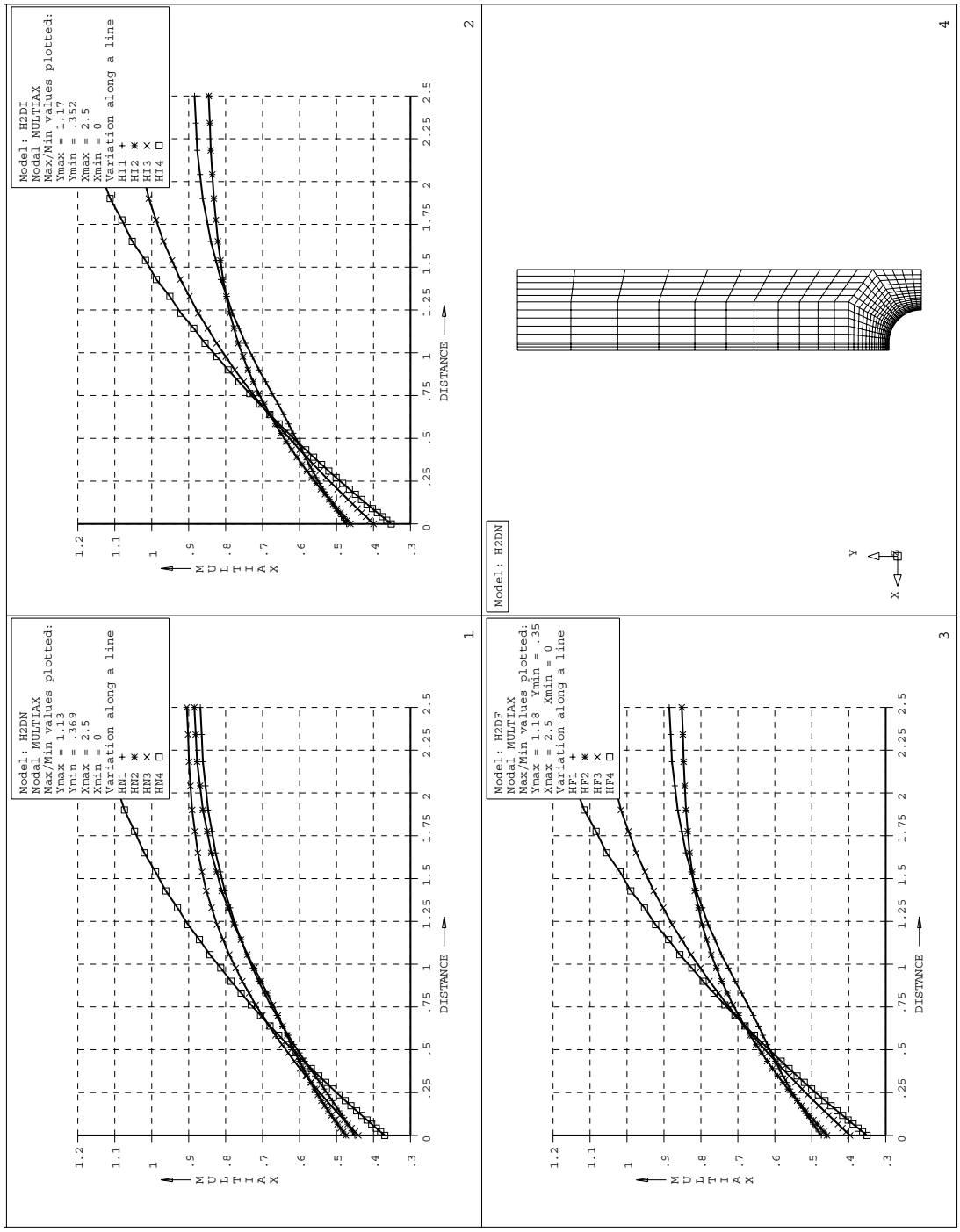

Figure 7: Triaxiality ratio (F82Hmod) at three temperature levels for a notch radius of 2mm.

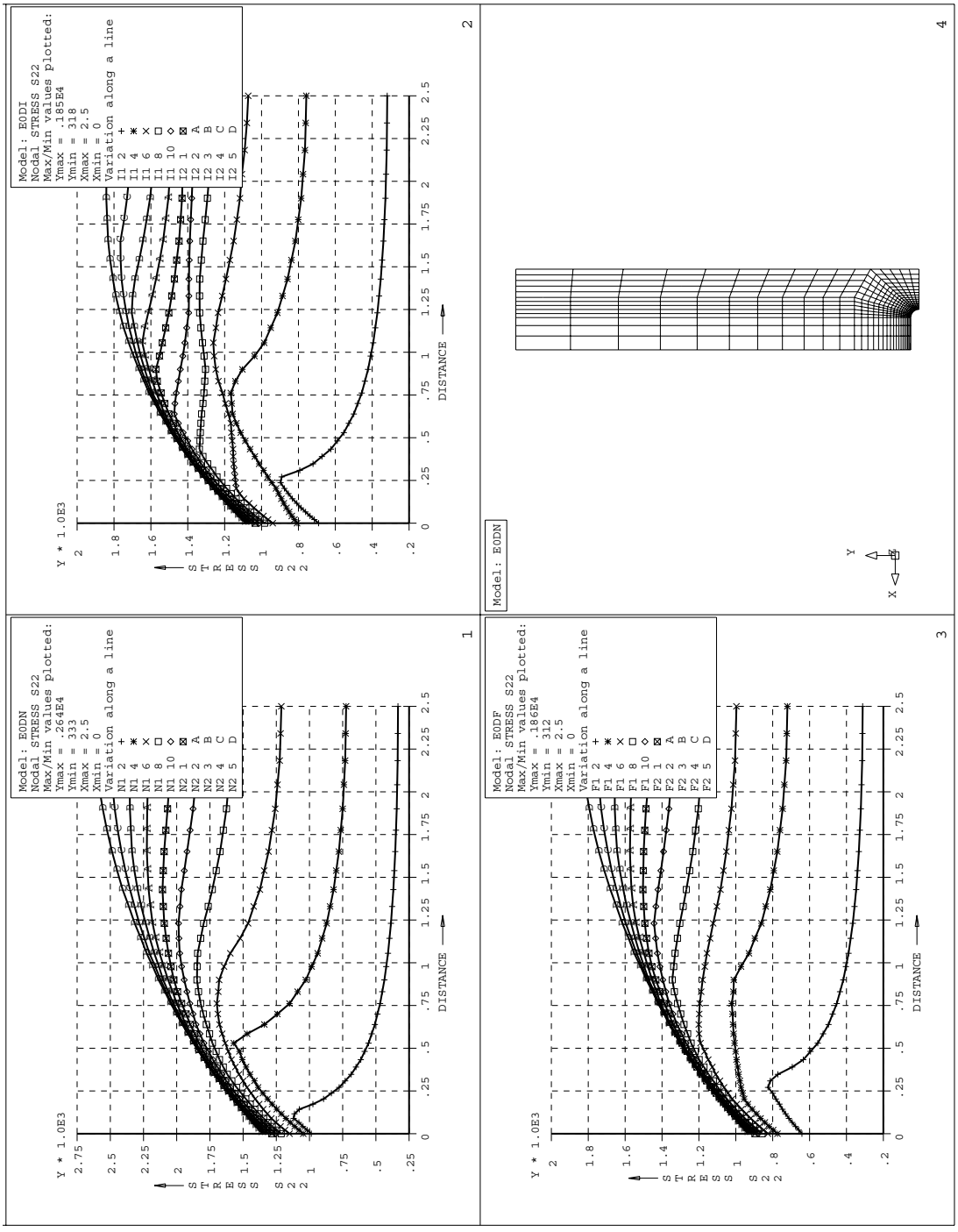

Figure 8: Axial stress distribution (EUROFER97) at three temperature levels for a notch radius of 0.5mm.

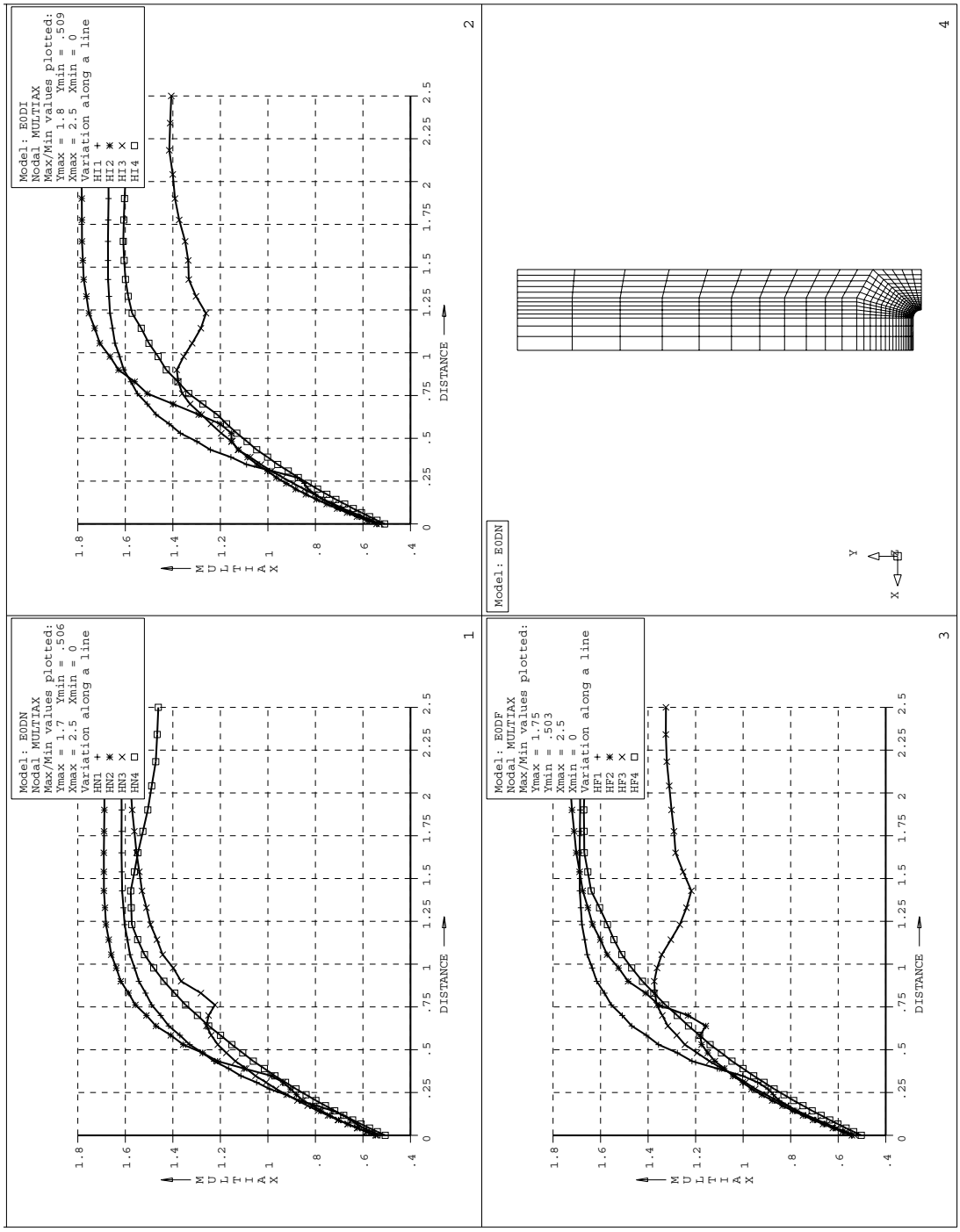

Figure 9: Triaxiality ratio (EUROFER97) at three temperature levels for a notch radius of 0.5mm.

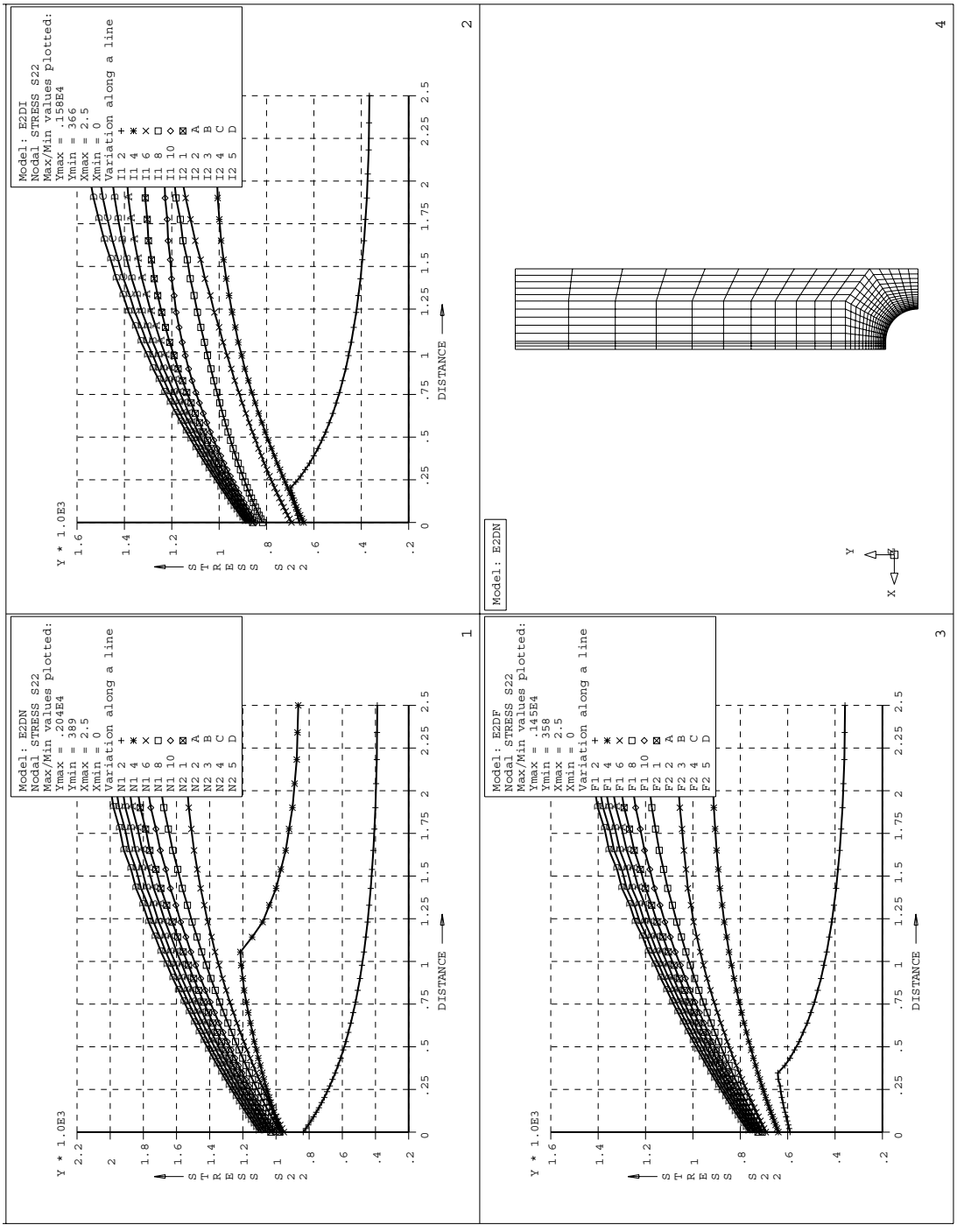

Figure 10: Axial stress distribution (EUROFER97) at three temperature levels for a notch radius of 2mm.

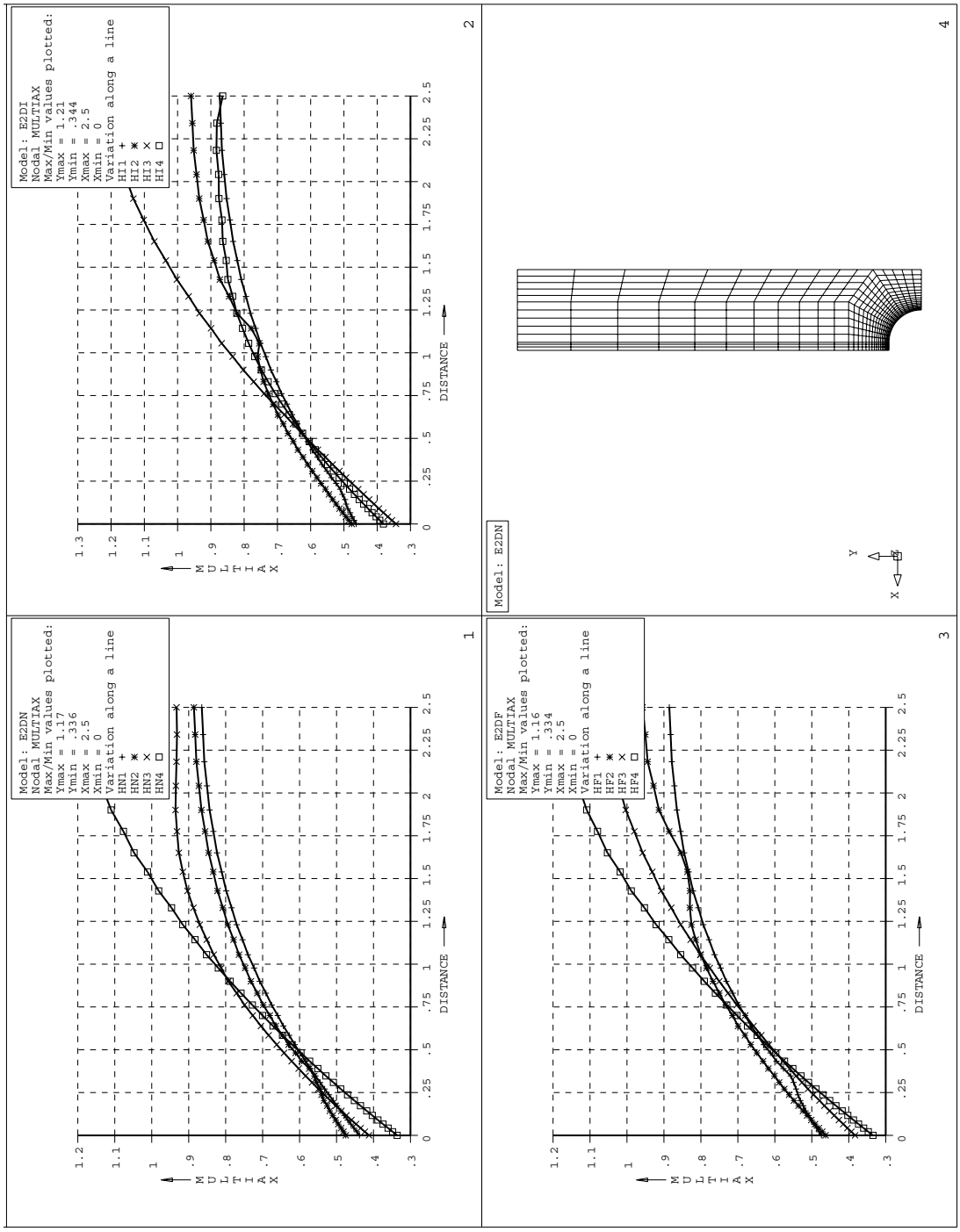

Figure 11: Triaxiality ratio (EUROFER97) at three temperature levels for a notch radius of 2mm.

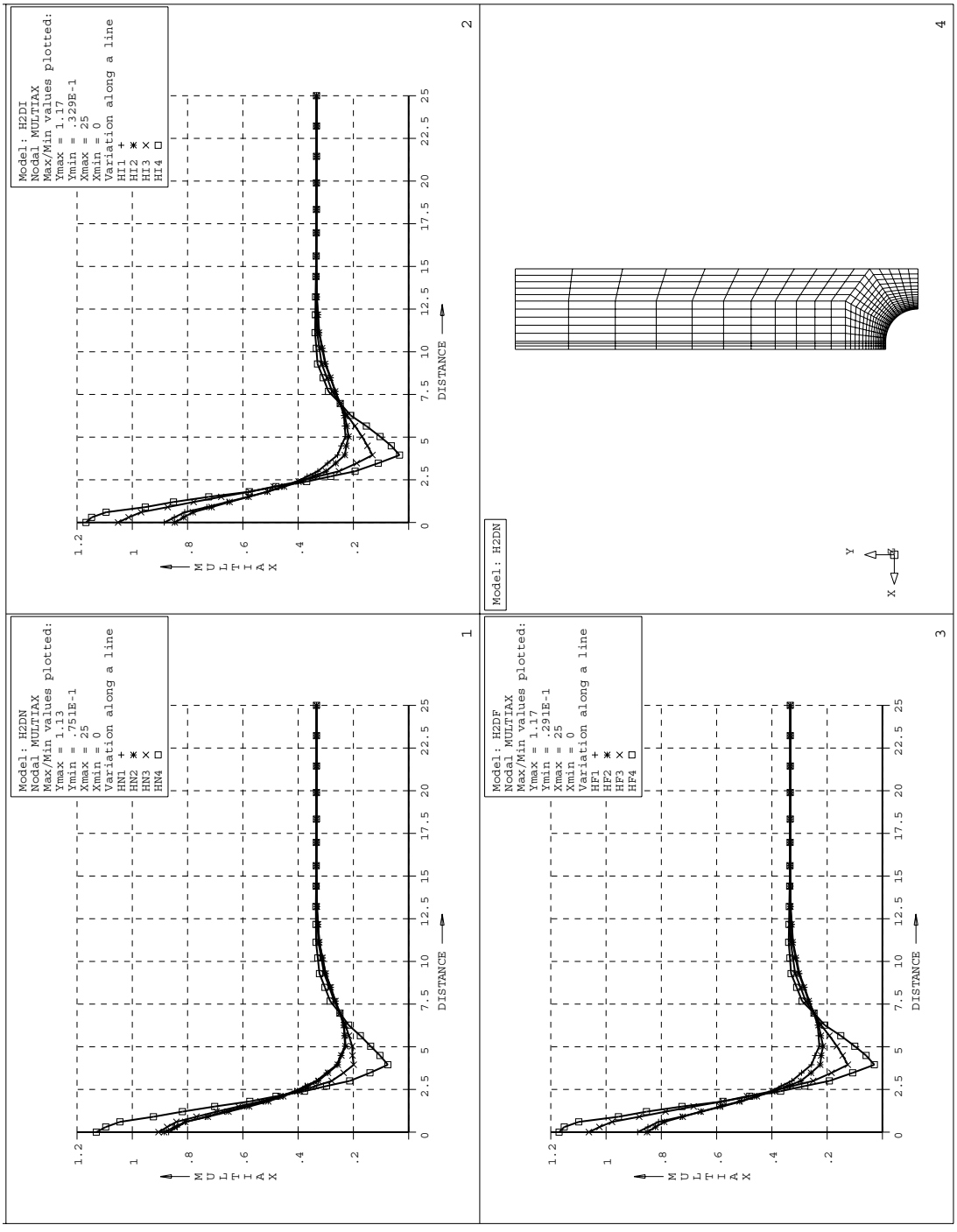

Figure 12: Triaxiality ratio (F82Hmod) along symmetry line at three temperature levels for a notch radius of 2mm.

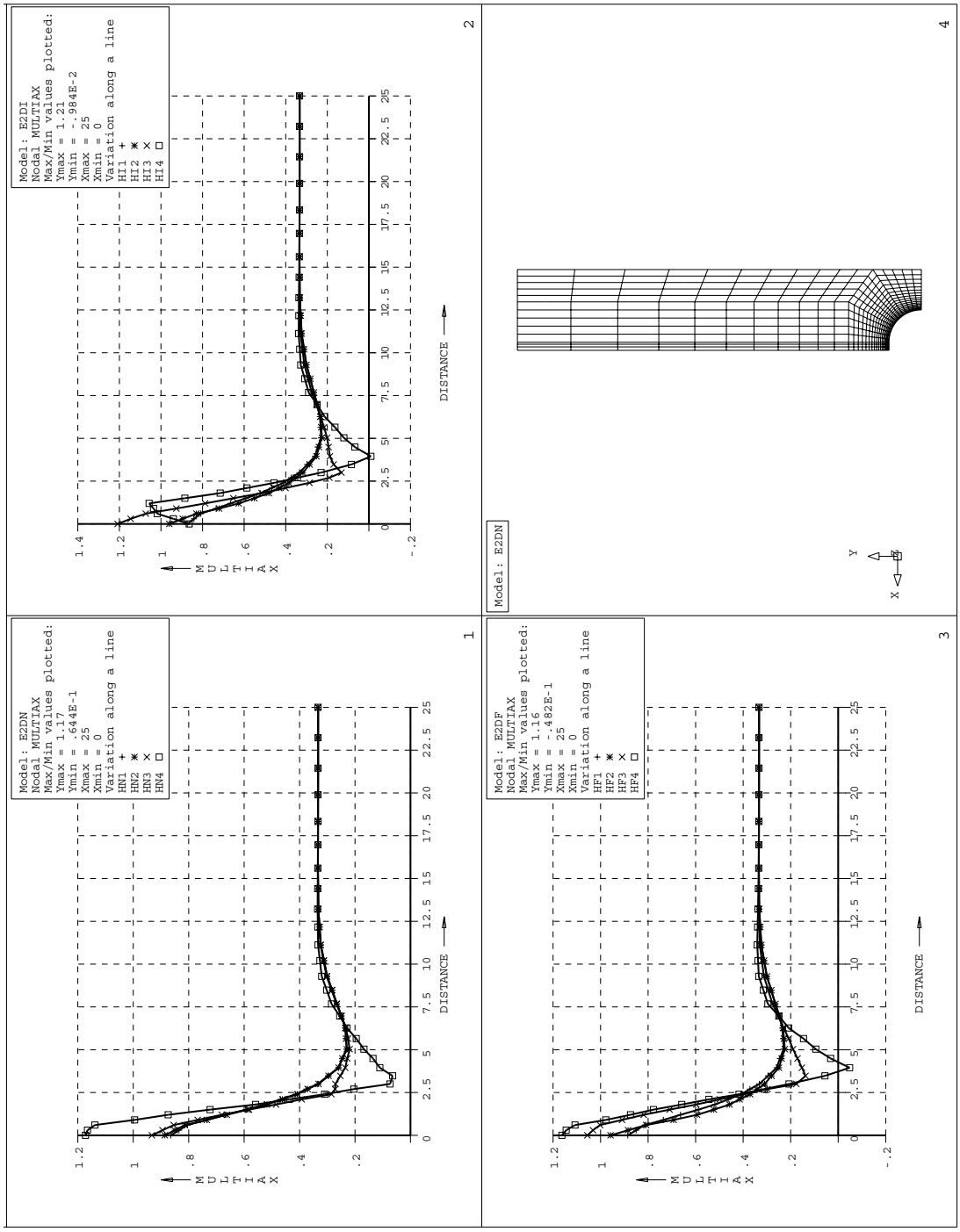

Figure 13: Triaxiality ratio (EUROFER97) along symmetry line at three temperature levels for a notch radius of 2mm.

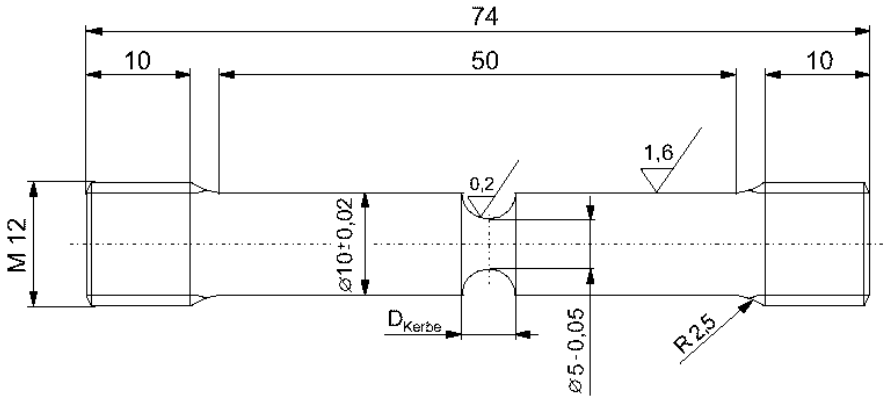

Figure 14: Geometry of axisymmetrically notched bar (RNB) specimens.

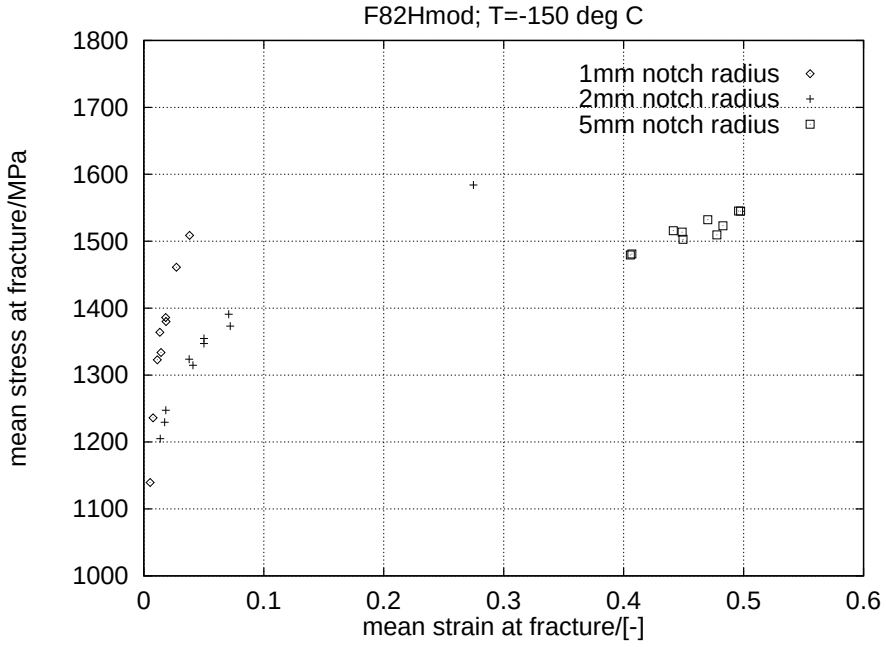

Figure 15: Mean stress σ_M and strain ε_M at fracture for F82Hmod (-150° C).

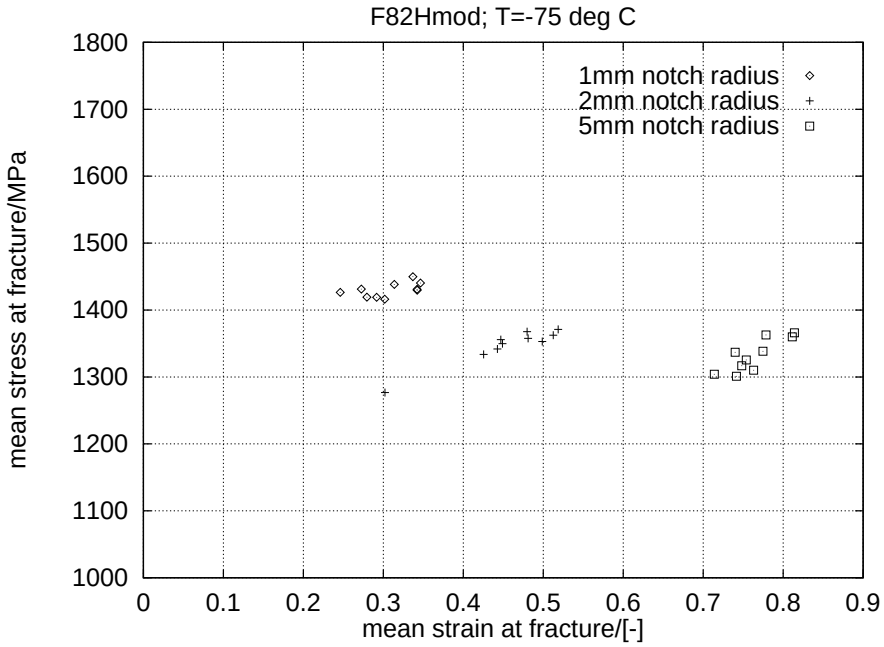

Figure 16: Mean stress σ_M and strain ε_M at fracture for F82Hmod (-75° C).

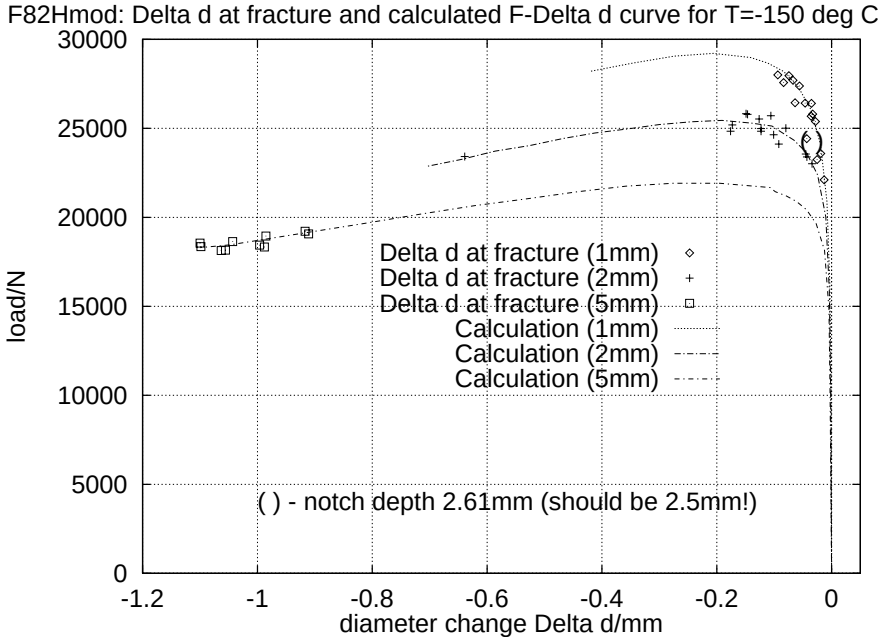

Figure 17: Results of the FE stress analysis together with the experimentally observed fracture loci for F82Hmod at -150° C.

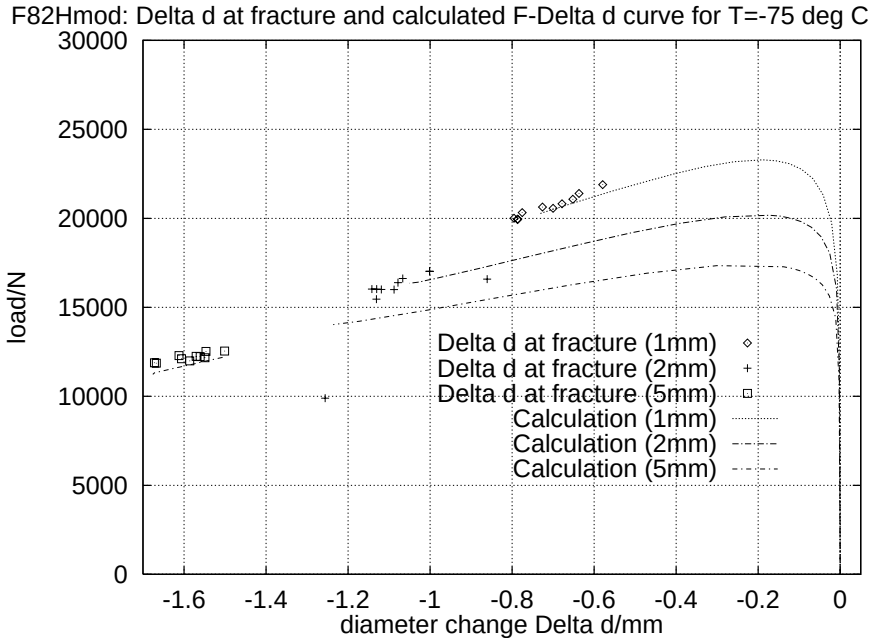

Figure 18: Results of the FE stress analysis together with the experimentally observed fracture loci for F82Hmod at -75° C.

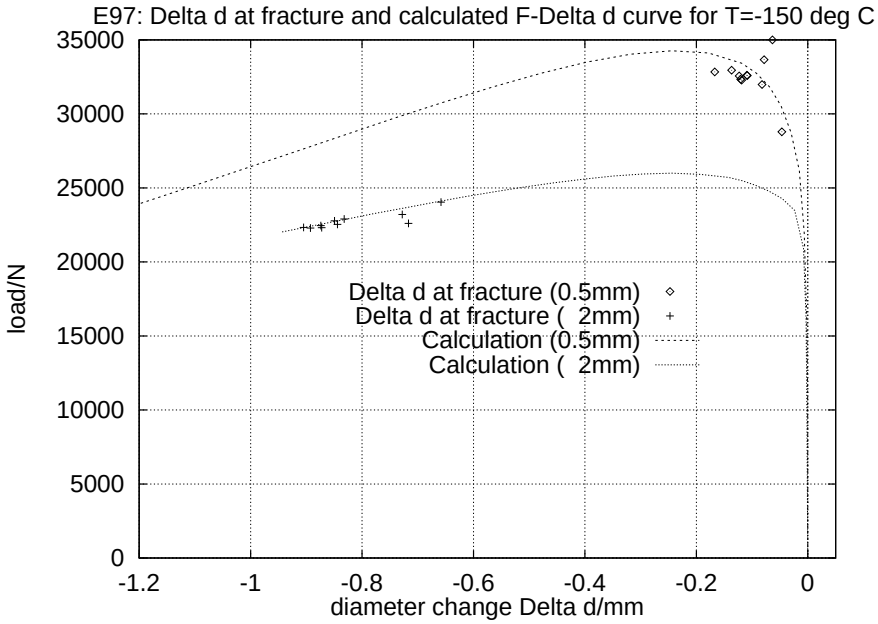

Figure 19: Results of the FE stress analysis together with the experimentally observed fracture loci for EUROFER97 at -150° C.

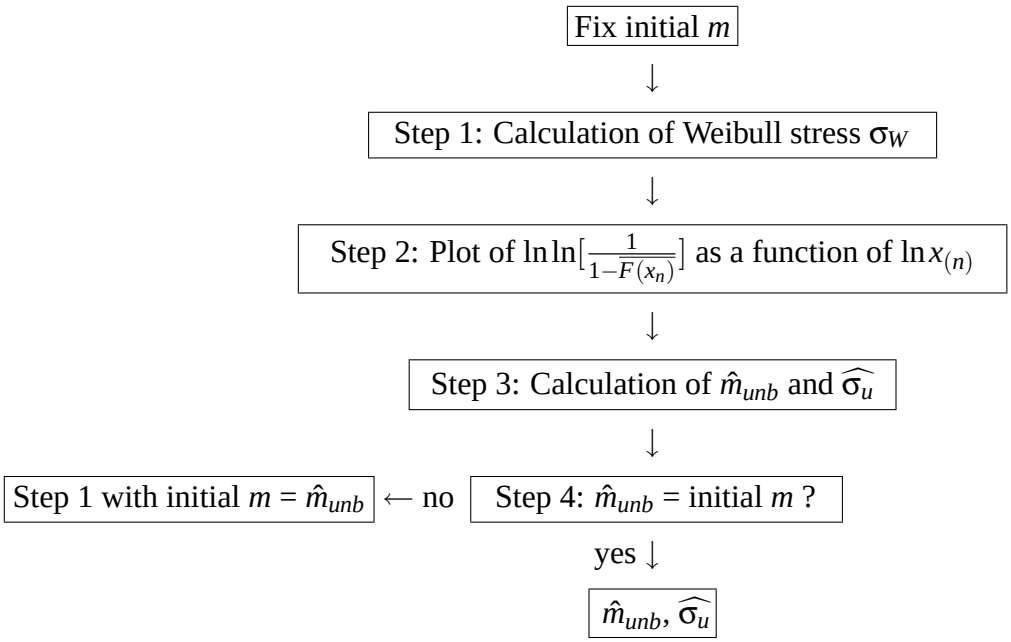

Figure 20: Flow diagram for iterative Weibull parameter estimation procedure.

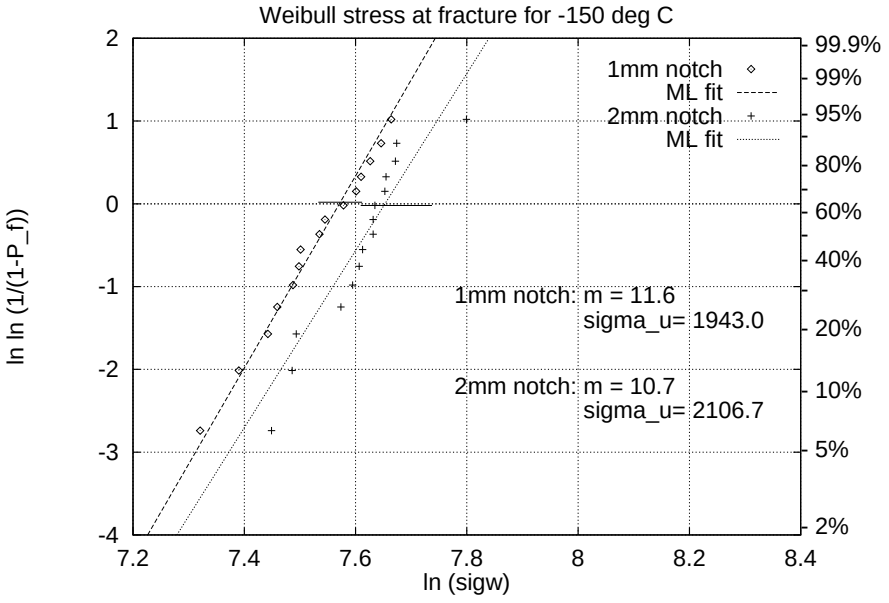

Figure 21: Results of Weibull stress calculation for -150° C(F82Hmod).

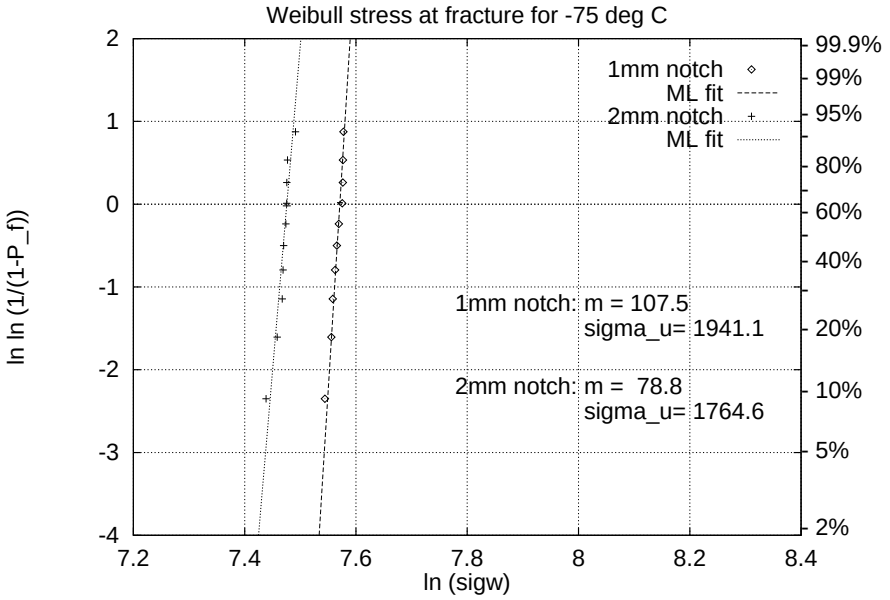

Figure 22: Results of Weibull stress calculation for -75° C(F82Hmod).

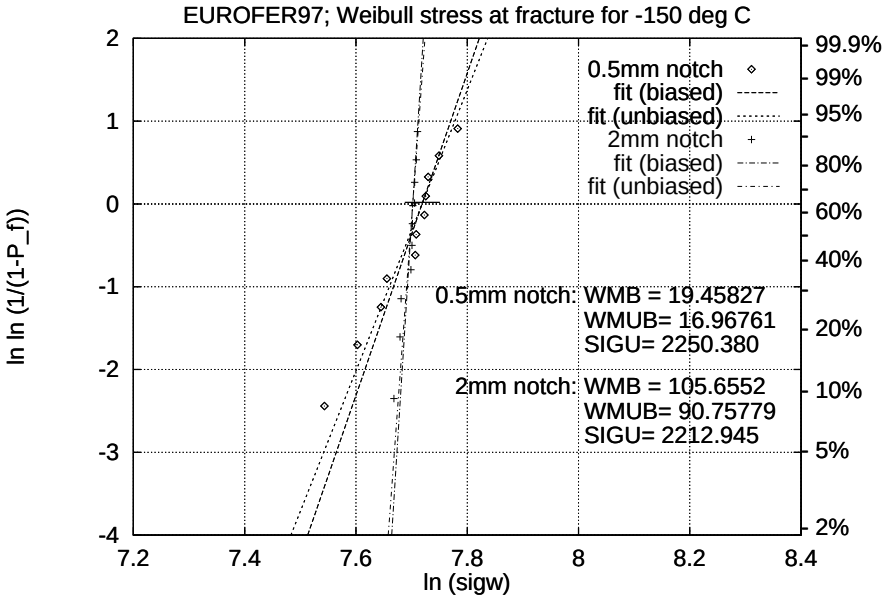

Figure 23: Results of Weibull stress calculation for -150° C(EUROFER97).

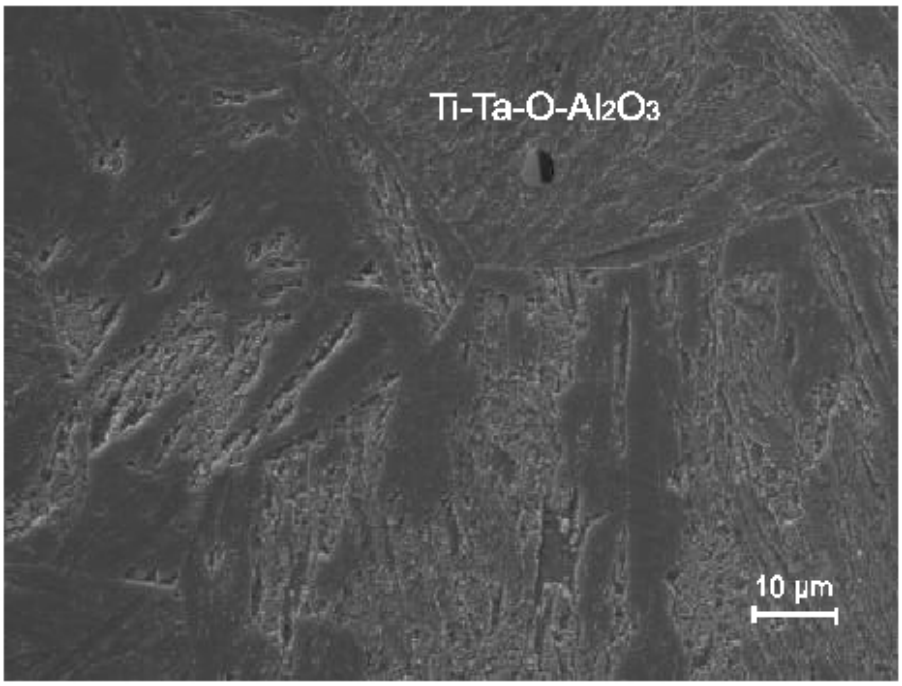

Figure 24: SEM section of F82Hmod in reference condition.

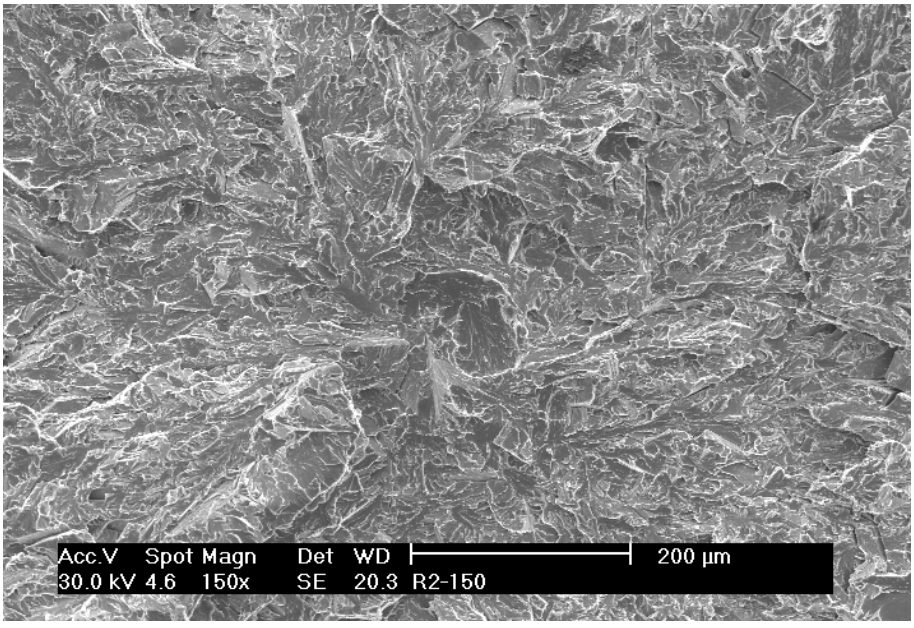

Figure 25: Fracture origin of $r = 2$mm notched F82Hmod specimen tested at $T = -150^{\circ}$C.

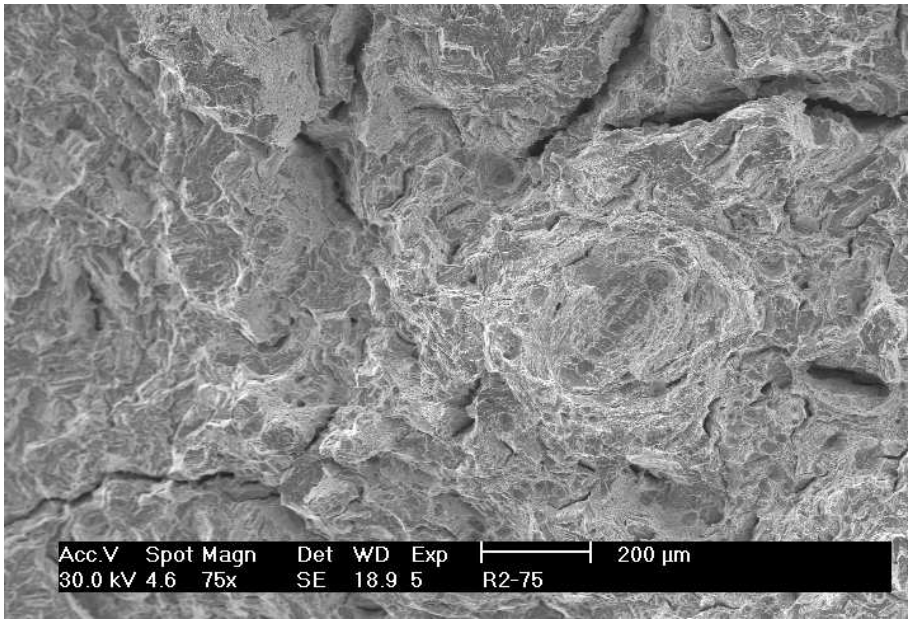

Figure 26: F82Hmod fracture surface of $r = 2$mm notched specimen tested at $T = -75^{\circ}$C.

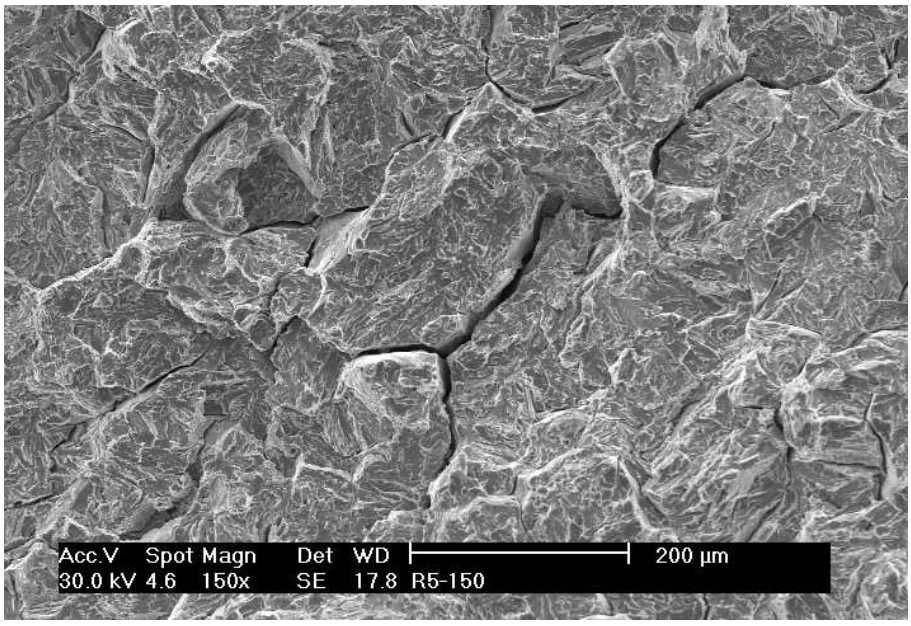

Figure 27: F82Hmod fracture surface of $r = 5$mm notched specimen tested at $T = -150^{\circ}$C .

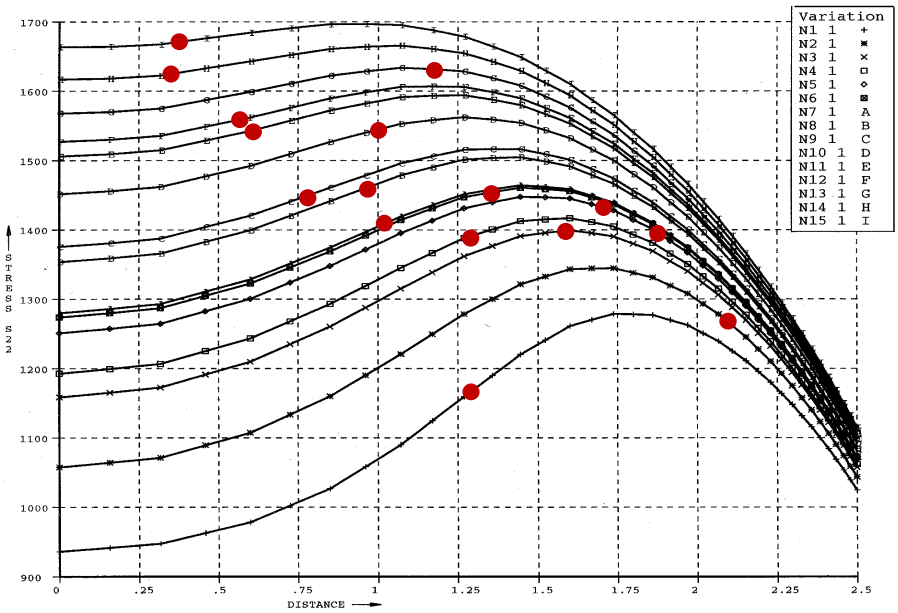

Figure 28: Results of finite element stress analysis for F82Hmod and corresponding fracture origin locations (distance from specimen centre of 1mm notched specimens) at -150° C.

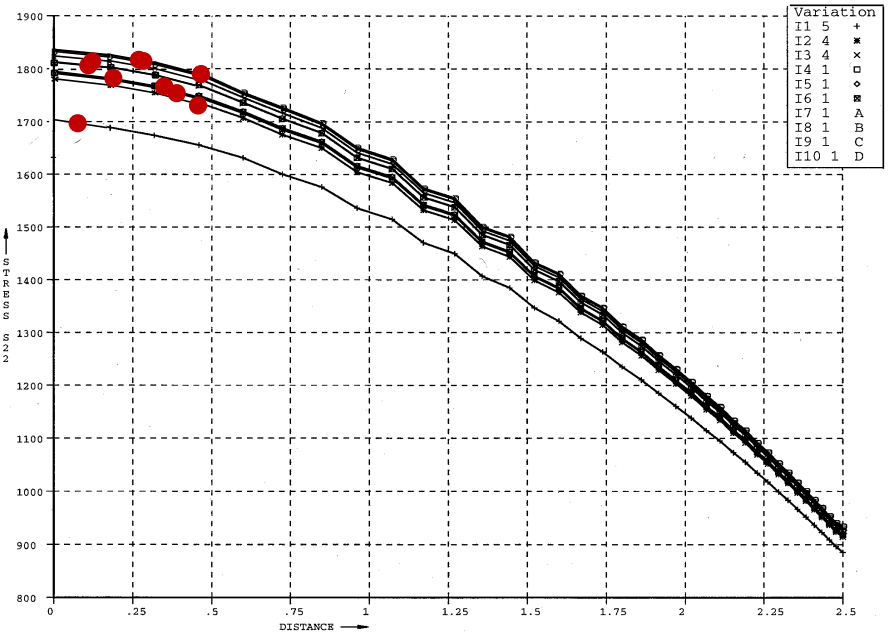

Figure 29: Results of finite element stress analysis for F82Hmod and corresponding fracture origin locations (distance from specimen centre of 2mm notched specimens) at -75° C.

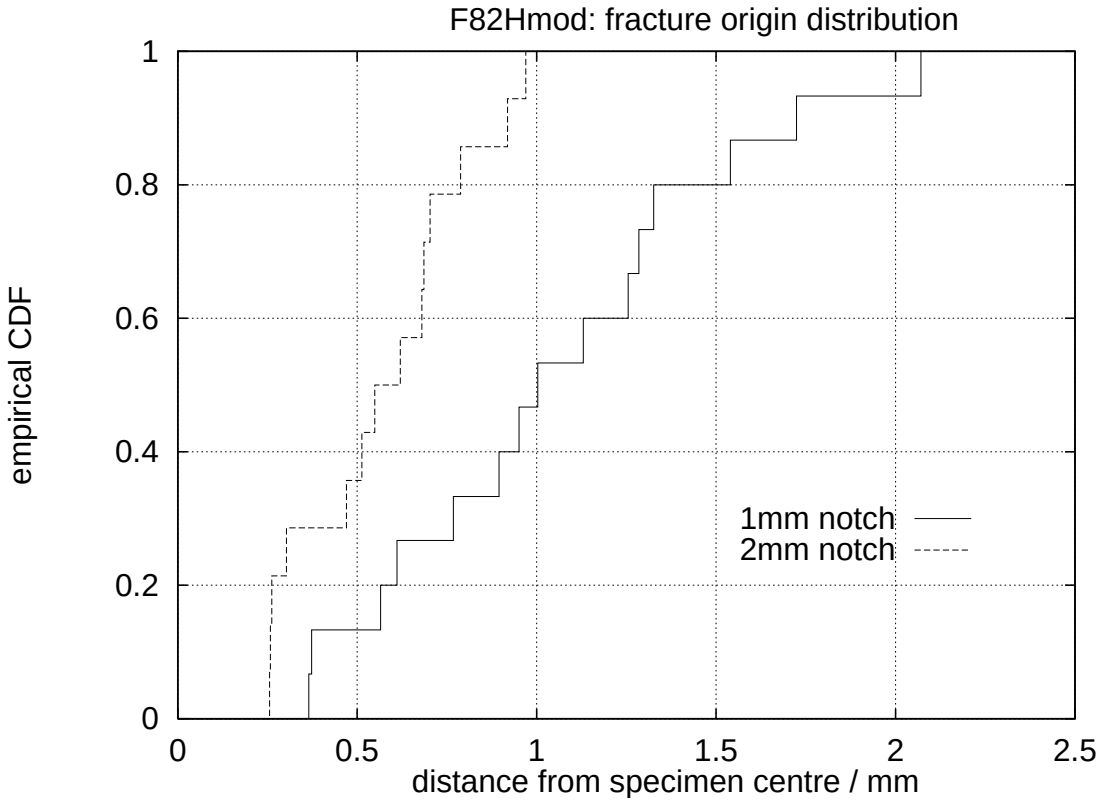

Figure 30: Fracture origin location distribution from fractography of 1 and 2mm notched F82Hmod specimens tested at -150° C.

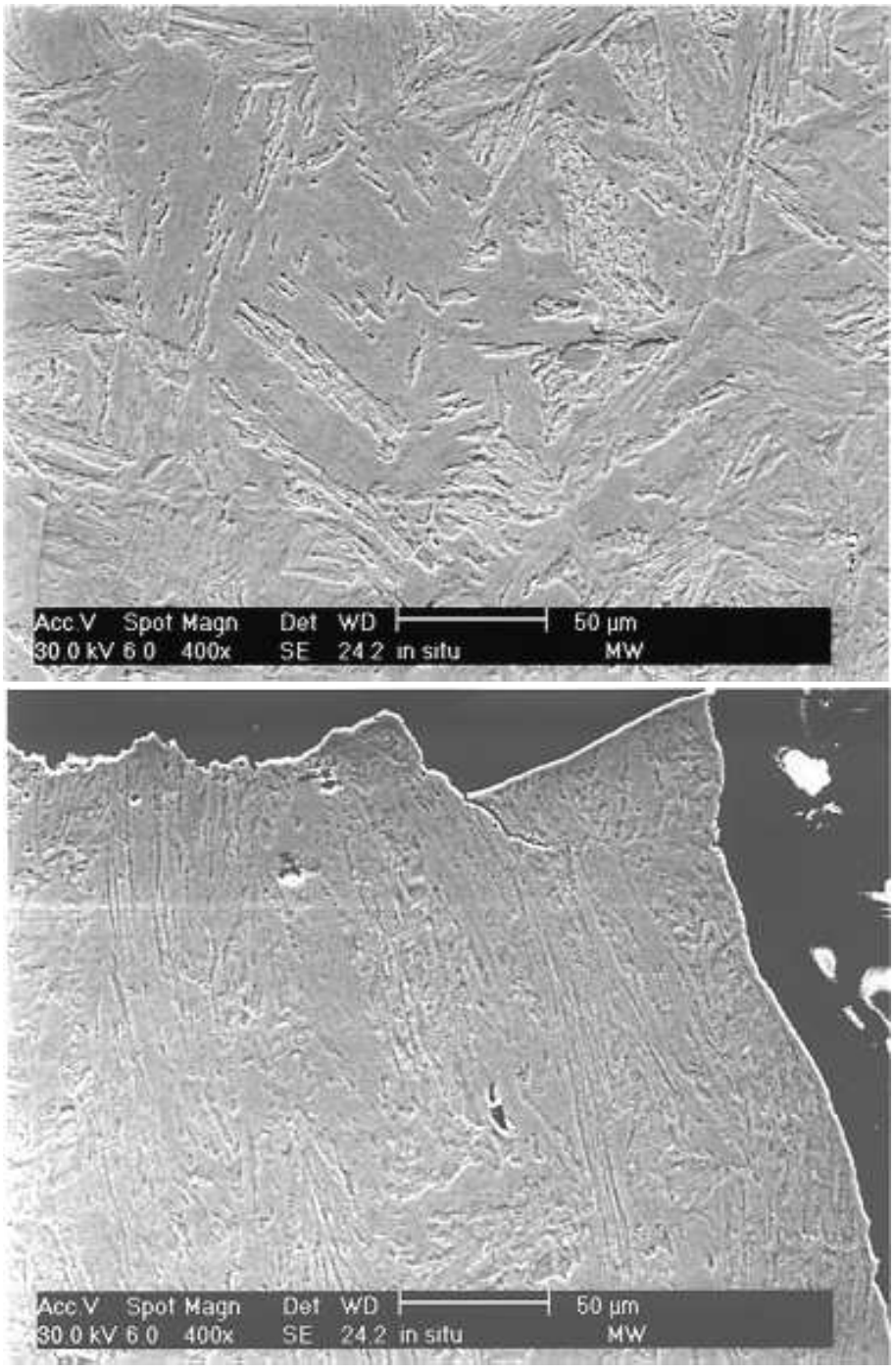

Figure 31: Orientation of martensite laths in undeformed (top) and deformed (bottom) part of the specimen.

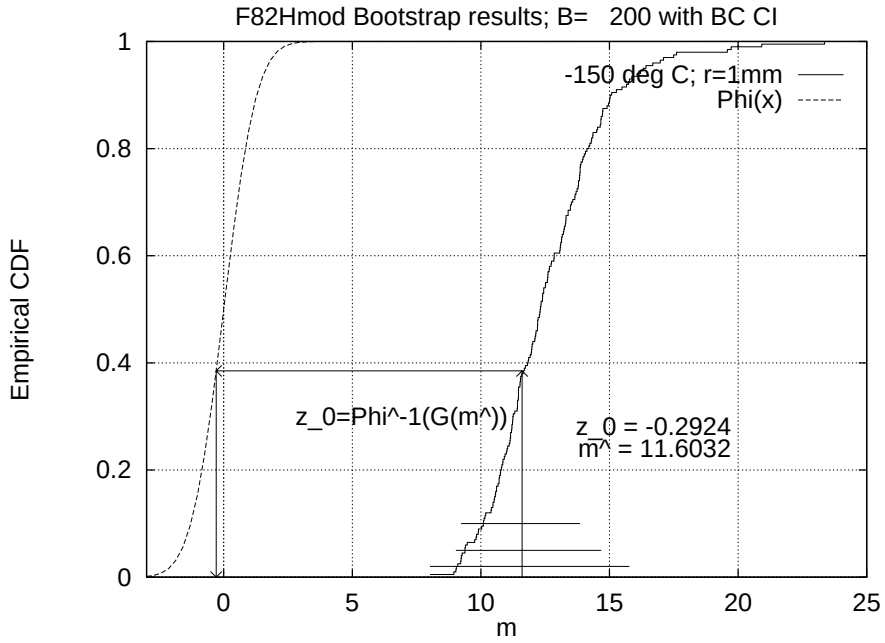

Figure 32: Empirical CDF and bootstrap confidence intervals for Weibull modulus *m* including determination of z_0^m.

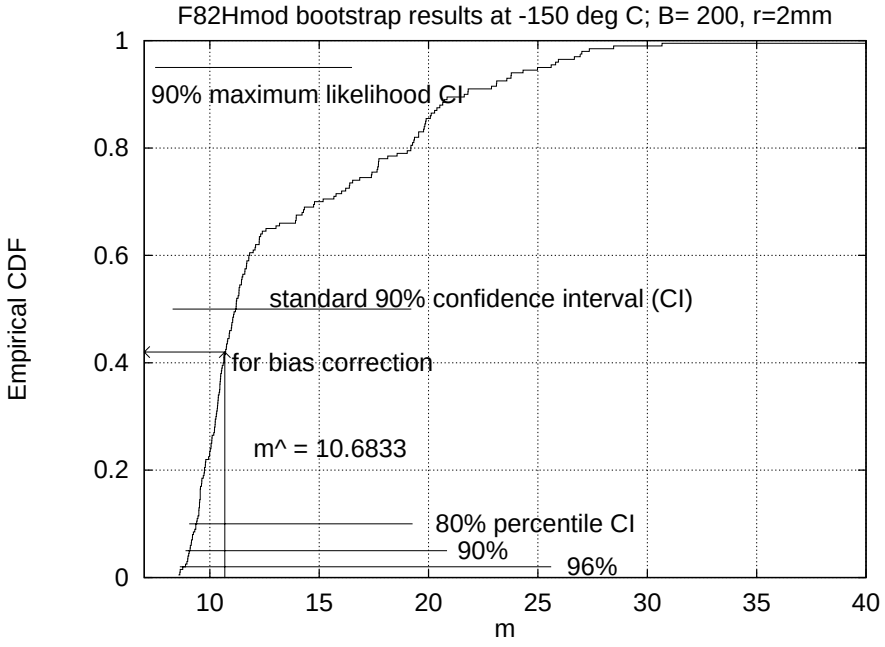

Figure 33: Empirical CDF and confidence intervals for Weibull modulus *m*.

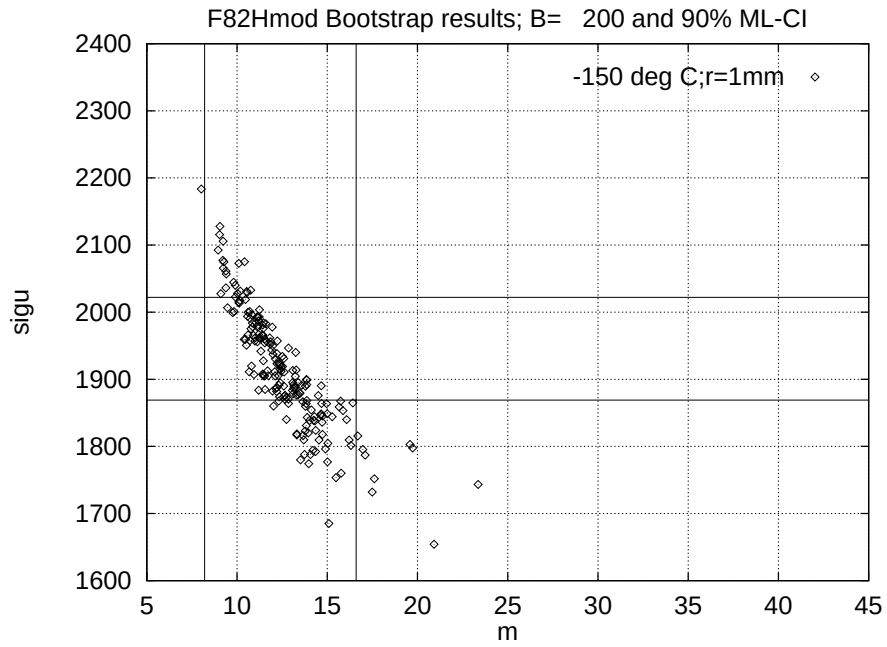

Figure 34: Results of $B = 200$ bootstrap replications for $(\hat{m}, \widehat{\sigma_u})$-pairs as scatterplot (Solid lines indicate 90% Maximum Likelihood confidence intervals).

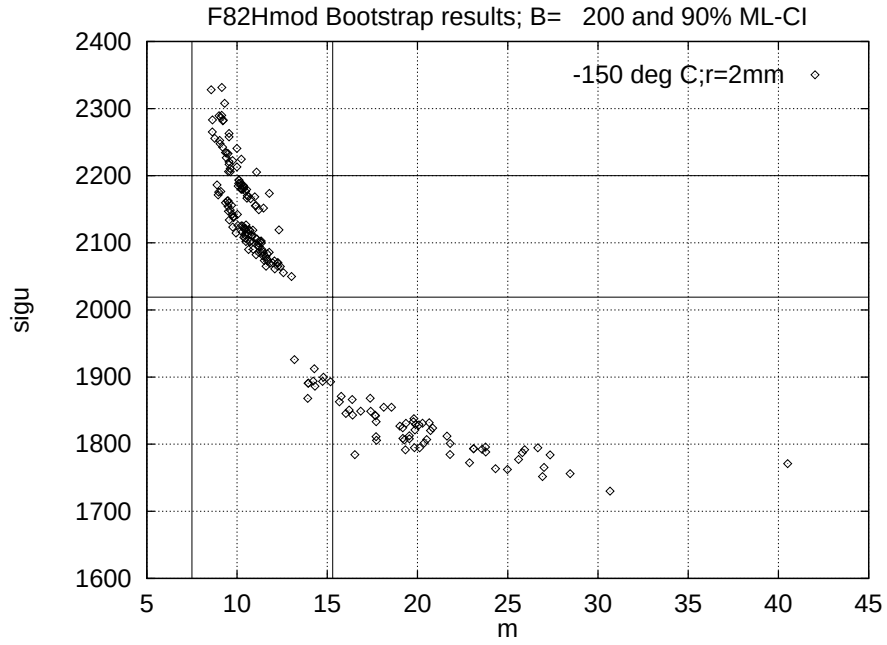

Figure 35: Results of $B = 200$ bootstrap replications for $(\hat{m}, \widehat{\sigma_u})$-pairs as scatterplot (Solid lines indicate 90% Maximum Likelihood confidence intervals).

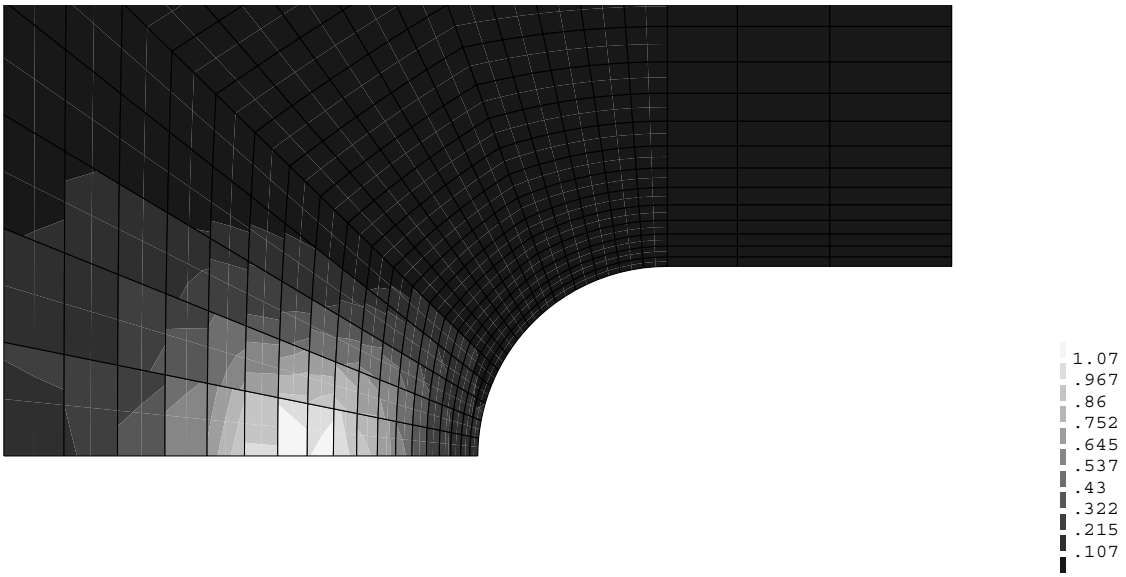

fracture origin probability density F82Hmod 1mm -150degC

Figure 36: Calculated fracture origin distribution for r=1mm notched F82Hmod specimen at -150° C.

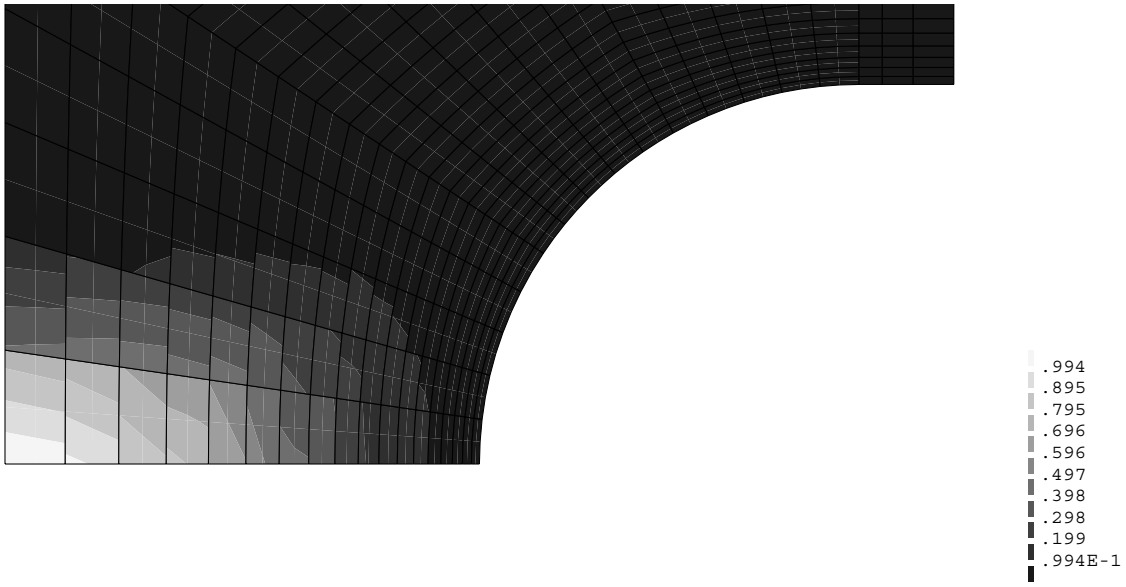

fracture origin probability density F82Hmod 2mm -150degC

Figure 37: Calculated fracture origin distribution for r=2mm notched F82Hmod specimen at -150° C.

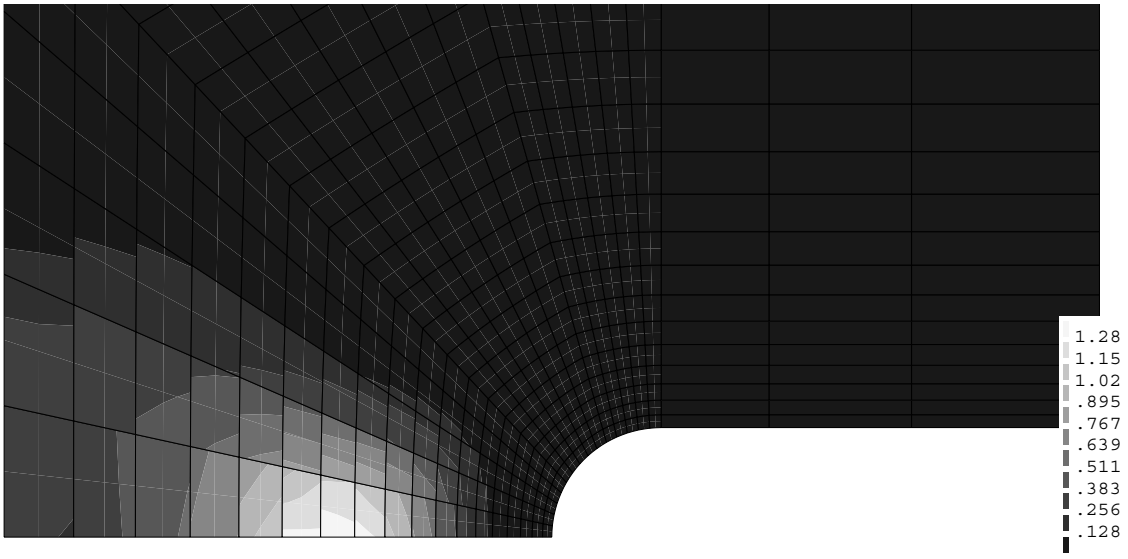

fracture origin probability density EUROFER97 0.5mm -150degC

Figure 38: Calculated fracture origin distribution for r=0.5mm notched EUROFER97 specimen at -150° C.

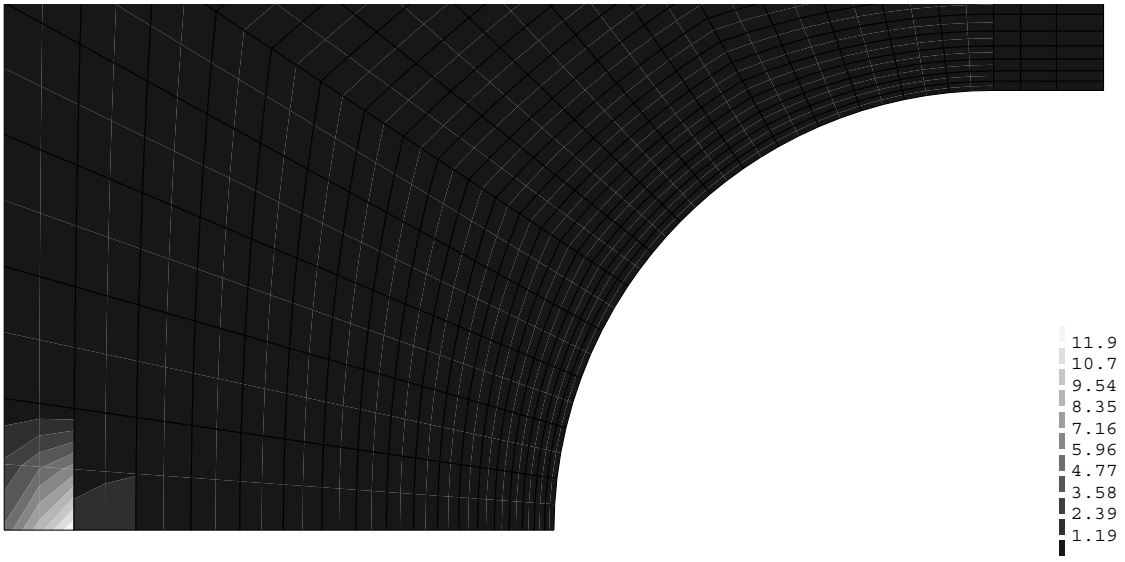

fracture origin probability density EUROFER97 2mm -150degC

Figure 39: Calculated fracture origin distribution for r=2mm notched EUROFER97 specimen at -150° C.

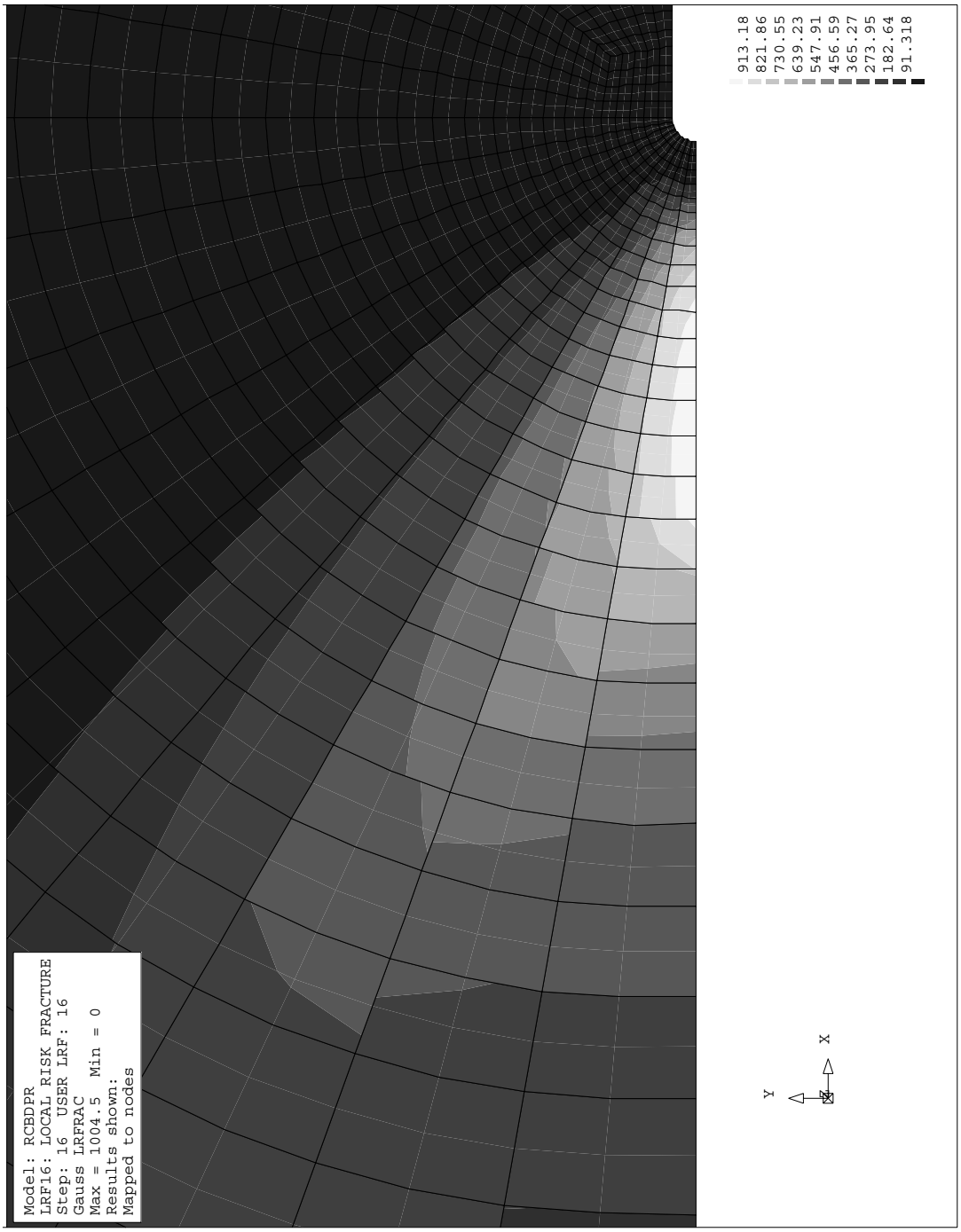

Figure 40: Local risk of rupture density for deeply pre-cracked F82Hmod specimen (parameters correspond to -150° C).

B Tables

basic composition:

Cr	C	Mn	P	S	V	B	N_2	O_2
7.7	0.09	0.16	0.002	0.002	0.16	0.0002	0.006	(0.01)

varied substitution elements:

W	Ta	Ti						
1.94	0.02	0.01						

radiologically undesired elements:

Nb	Mo	Ni	Cu	Al	Si	Co	Sn	As
0.0001	< 0.0030	0.020	0.01	0.003	0.11	0.005	(< 0.002)	(< 0.005)

Table 1: Composition (wt-%) of F82Hmod; Heat No. 9741

basic composition:

Cr	C	Mn	P	S	V	B	N_2	O_2
8.82	0.11	0.47	0.005	0.004	0.20	< 0.0010	0.020	0.0010

varied substitution elements:

W	Ta	Ti						
1.09	0.13	0.005						

radiologically undesired elements:

Nb	Mo	Ni	Cu	Al	Si	Co	Sn	As
0.0016	< 0.0010	0.020	0.0016	0.009	0.04	0.006	< 0.005	< 0.005

Table 2: Composition (wt-%) of EUROFER 97; Heat No. E83689

RT				-75° C				-150° C			
K	σ_0	E	n	K	σ_0	E	n	K	σ_0	E	n
820	520	214000	0.07	950	570	240000	0.07	1200	810	220000	0.07

Table 3: F82Hmod material parameters K, σ_0 (0.2% offset yield strength), E (units are MPa), and n.

RT				-75° C				-150° C			
K	σ_0	E	n	K	σ_0	E	n	K	σ_0	E	n
880	526	202000	0.08	1030	593	208000	0.09	1290	855	222000	0.09

Table 4: EUROFER97 material parameters K, σ_0 (0.2% offset yield strength), E (units are MPa), and n.

Spec #	Δd/mm	F/N	ε_M/[-]	σ_M/MPa	σ_W/MPa
1	-.06720	27699.3	.02706	1449.41	2017.932
2	-.09365	28003.9	.03782	1481.19	2130.225
3	-.01305	22105.5	.00523	1131.72	1511.097
4	-.01899	23585.9	.00761	1210.40	1620.141
5	-.04330	24424.8	.01740	1265.77	1872.734
6	-.04600	26416.0	.01849	1370.46	1891.322
7	-.03300	25804.7	.01324	1331.74	1785.756
8	-.02801	25383.8	.01124	1307.39	1736.102
9	-.03568	25679.7	.01432	1326.72	1810.252
10	-.03512	26402.0	.01410	1363.73	1805.072
11	-.02535	23247.1	.01017	1196.06	1707.088
12	-.08363	27569.3	.03373	1452.27	2091.874
13	-.06376	26438.6	.02567	1381.52	2000.325
14	-.05597	27380.7	.02251	1426.24	1955.193
15	-.07432	27964.8	.02995	1467.54	2051.550

Table 5: Results for F82Hmod 1mm notched specimens tested at -150 $^\circ$C.

```
     467    1496   810.0     No. of elems / nodes;  FLOW STRESS FOR IPFLAG
    1    1    2   21   20  115  134  152  133   CAX8R
    2    2    3   22   21  116  135  153  134   CAX8R
    3    3    4   23   22  117  136  154  135   CAX8R
.
```

. (FE contiguity list and ABAQUS element type)

```
.
  467 1381 1212 1217 1386 1486 1322 1496 1491   CAX8R
    1   0.0000000E+00   0.0000000E+00
    2   0.3174896       0.0000000E+00
    3   0.5994086       0.0000000E+00
.
```

. (FE nodal coordinates)

```
.
 1496    1.575000        25.00000
H1WN: RNB with dmin=5 d=10 r=1 l=50 for Weibull analysis at -150 deg C (=N)
           START OF NEW INCREMENT
    1     940.9080       947.0146       947.7156       953.1441     1111
    2     955.9350       973.1522       960.9180       977.0444     1111
    3     989.4988       1016.502       992.0236       1017.019     1111
.
```

.(element No. and max. 1st principal stress at 4 Gauss-points; plastic zone flag at 4 Gauss-points)

```
.
  467     361.7161       361.7152       361.7098       361.7091     0000
(END)
```

Table 6: Part of the auxiliary `*.wst`-file.

```
 ************************************************
 WSTRIT: ******* ITERATION #  1  STARTING *******
 ************************************************
 SUBROUTINE PSENV...
  ===> analyse file : /v1/home/imf2/riesch/netze/f82hmod/h1wn
                      WITH SIG0=  8.1E+2
  ===> which is assumed to contain  15  loadstep results
 READING FROM FORTRAN UNIT  33
 2 -DIMENSIONAL ANALYSIS   8  NODES AND  4  INTEGRATION POINTS PER ELEMENT
     467    1496   810.0
 ELEM. #     1 TYPE: CAX8R    NODES:     1     2    21    20
  115   134   152   133
 ELEM. #     2 TYPE: CAX8R    NODES:     2     3    22    21
  116   135   153   134
 ELEM. #     3 TYPE: CAX8R    NODES:     3     4    23    22
  117   136   154   135
.
.
.
 ELEM. #   467 TYPE: CAX8R    NODES:  1381  1212  1217  1386
 1486  1322  1496  1491
 NODE  #     1 COORDS:   0.000000       0.000000
 NODE  #     2 COORDS:  0.3174896       0.000000
 NODE  #     3 COORDS:  0.5994086       0.000000
.
.
.
 NODE  #  1496 COORDS:   1.575000       25.00000
INT2WS: INTEL, WSTR=    1   1.888
INT2WS: INTEL, WSTR=    2   3.929
INT2WS: INTEL, WSTR=    3   6.797
.
.
.
INT2WS: INTEL, WSTR=  467   353.4
 INT2WS: LOADSTEP 1
 467  ELEMENTS PROCESSED
 CALCULATED WEIBULL STRESS: 1.19775531372391117955527490216E+3
 SIZE OF PLASTIC ZONE: 1.68388519104661616115423407862E+1
 TOTAL SPECIMEN SIZE: 1.22714596552909986666666666264E+2
 FRACTION OF PLASTIC ZONE ===> 0.1372
 INT2WS FINISHED...
```

Table 7: Part of the Weibull stress results file.

```
. . .
 INT2WS: LOADSTEP 15
 467  ELEMENTS PROCESSED
 CALCULATED WEIBULL STRESS: 1.68119133063824927455344465683E+3
 SIZE OF PLASTIC ZONE: 2.24256528267552753517089936911E+1
 TOTAL SPECIMEN SIZE: 1.22714596552909986666666666264E+2
 FRACTION OF PLASTIC ZONE ===> 0.1827
 INT2WS FINISHED...


          SUMMARY
          =======


 INPUT FILE: /v1/home/imf2/riesch/netze/f82hmod/h1wn

 STRESSES NORMALIZED BY FLOW STRESS  810.0000
 WEIBULL MODULUS:      15.00

 SYMMETRY FACTOR:      12.57
 LOAD STEP     WEIBULL STRESS
    1            1417.910
    2            1514.080
    3            1592.243
    4            1618.642
    5            1664.174
    6            1682.003
    7            1686.794
    8            1744.928
    9            1762.338
   10            1822.536
   11            1865.406
   12            1882.202
   13            1914.378
   14            1953.152
   15            1990.205

WSTRIT: WMUB=    11.55341     SIGU=    1812.764
. . .
```

Table 7: Part of the Weibull stress results file (cont'd.).

```
 ************************************************
 WSTRIT: ******* ITERATION #  2  STARTING *******
 ************************************************
.
.
.
 WSTRIT: CONVERGENCE ACHIEVED AFTER  2  STEPS
         TOLERANCE FOR WMB-WM0:  1.E-1
        WM(UNBIASED)=    11.60445     WM(BIASED)=    12.78024


   *********** CONFIDENCE LIMITS ... ******************

 CONFIDENCE-LIMITS FOR ML ESTIMATES (SAMPLE SIZE =   15):

 CONFIDENCE-LEVEL: 80%

        M       :  [     8.956016 ,    15.528840 ]
        SIGU    :  [  1886.991505 ,  2003.705685 ]

 CONFIDENCE-LEVEL: 90%

        M       :  [     8.171506 ,    16.597708 ]
        SIGU    :  [  1868.625319 ,  2021.975136 ]

 CONFIDENCE-LEVEL: 96%

        M       :  [     7.378889 ,    17.849491 ]
        SIGU    :  [  1846.243770 ,  2044.566384 ]

  *********** ... CONFIDENCE LIMITS ******************
```

Table 7: Part of the Weibull stress results file (cont'd.).

```
  GENERATING GNUPLOT DATAFILE...

# PLOT: GENERATE PLOTFILE FOR ML RESULTS ( AT THE MOMENT: GNUPLOT-FORMAT)
#  RESULTS FROM .wst-FILE: /v1/home/imf2/riesch/netze/f82hmod/h1wn

#  SIGU=   1943.028       WMB =   12.78024       WMUB=   11.60445
#  LN(SIGW)    LN LN 1/(1-FI)    SIGW        FI
   7.320591        -2.740493         1511.097        0.6250000E-01
   7.390268        -2.013419         1620.141        0.1250000
   7.442544        -1.571953         1707.088        0.1875000
   7.459398        -1.245899         1736.102        0.2500000
   7.487597       -0.9816471         1785.756        0.3125000
   7.498356       -0.7550149         1805.072        0.3750000
   7.501221       -0.5527521         1810.252        0.4375000
   7.535155       -0.3665129         1872.734        0.5000000
   7.545031       -0.1903393         1891.322        0.5625000
   7.578244       -0.1935689E-01     1955.193        0.6250000
   7.601065        0.1511325         2000.325        0.6875000
   7.626351        0.5152019         2051.550        0.8125000
   7.645816        0.7320994         2091.874        0.8750000
   7.663983         1.019781         2130.225        0.9375000
# MLPLOT: PLOTFILE GENERATED...
# COLS ARE: LN(SIGW(I)),LN LN 1/1-FI,SIGW(I),FI

  WSTRIT TERMINATED SUCCESSFULLY...

(END)
```

Table 7: Part of the Weibull stress results file (cont'd.).

		m	90% ML-CI	σ_u	90% ML-CI
$T = -150°C$	$r = 1$mm	11.6	[8.2, 16.6]	1943.0	[1868.6, 2022.0]
	$r = 2$mm	10.7	[7.5, 15.3]	2106.7	[2019.3, 2199.7]
	$r = 5$mm	78.9	[50.8, 124.5]	1913.2	[1899.9, 1927.1]
$T = -75°C$	$r = 1$mm	107.5	[69.2, 169.5]	1941.1	[1927.9, 1954.7]
	$r = 2$mm	78.8	[50.8, 124.3]	1764.6	[1752.2, 1777.4]
	$r = 5$mm	–	–	–	–

Table 8: Maximum likelihood results for σ_W-parameters (F82Hmod, V_0=1mm^3).

		m	90% ML-CI	σ_u	90% ML-CI
$T = -150°C$	$r = 0.5$mm	17.0	[11.2, 26.1]	2250.4	[2181.5, 2323.5]
	$r = 2$mm	90.8	[58.5, 143.2]	2212.9	[2199.5, 2226.9]

Table 9: Maximum likelihood results for σ_W-parameters (EUROFER97, V_0=1mm^3).

N	$b(N)$
5	0.669
6	0.752
7	0.792
8	0.820
9	0.842
10	0.859
11	0.872
12	0.883
13	0.893
14	0.901
15	0.908
16	0.914

N	$b(N)$
17	0.919
18	0.923
19	0.927
20	0.931
21	0.935
22	0.938
23	0.941
24	0.943
25	0.945
26	0.947
27	0.949
28	0.951

N	$b(N)$
29	0.953
30	0.955
31	0.957
32	0.958
33	0.959
34	0.960
35	0.961
36	0.962
37	0.963
38	0.964
39	0.965
40	0.966

Table 10: Unbiasing factors $b(N)$

N	$\alpha_1 = 0.02$	$\alpha_1 = 0.05$	$\alpha_1 = 0.10$	$\alpha_2 = 0.90$	$\alpha_2 = 0.95$	$\alpha_2 = 0.98$
5	-1.631	-1.247	-0.888	0.772	1.107	1.582
6	-1.396	-1.007	-0.74	0.666	0.939	1.291
7	-1.196	-0.874	-0.652	0.598	0.829	1.12
8	-1.056	-0.784	-0.591	0.547	0.751	1.003
9	-0.954	-0.717	-0.544	0.507	0.691	0.917
10	-0.876	-0.665	-0.507	0.475	0.644	0.851
11	-0.813	-0.622	-0.477	0.448	0.605	0.797
12	-0.762	-0.587	-0.451	0.425	0.572	0.752
13	-0.719	-0.557	-0.429	0.406	0.544	0.714
14	-0.683	-0.532	-0.41	0.389	0.52	0.681
15	-0.651	-0.509	-0.393	0.374	0.499	0.653
16	-0.624	-0.489	-0.379	0.36	0.48	0.627
17	-0.599	-0.471	-0.365	0.348	0.463	0.605
18	-0.578	-0.455	-0.353	0.338	0.447	0.584
19	-0.558	-0.441	-0.342	0.328	0.433	0.566
20	-0.54	-0.428	-0.332	0.318	0.421	0.549
22	-0.509	-0.404	-0.314	0.302	0.398	0.519
24	-0.483	-0.384	-0.299	0.288	0.379	0.494
26	-0.46	-0.367	-0.286	0.276	0.362	0.472
28	-0.441	-0.352	-0.274	0.265	0.347	0.453
30	-0.423	-0.338	-0.264	0.256	0.334	0.435
32	-0.408	-0.326	-0.254	0.247	0.323	0.42
34	-0.394	-0.315	-0.246	0.239	0.312	0.406
36	-0.382	-0.305	-0.238	0.232	0.302	0.393
38	-0.37	-0.296	-0.231	0.226	0.293	0.382
40	-0.36	-0.288	-0.224	0.22	0.285	0.371
42	-0.35	-0.28	-0.218	0.214	0.278	0.361
44	-0.341	-0.273	-0.213	0.209	0.271	0.352
46	-0.333	-0.266	-0.208	0.204	0.264	0.344
48	-0.325	-0.26	-0.203	0.199	0.258	0.336
50	-0.318	-0.254	-0.198	0.195	0.253	0.328
52	-0.312	-0.249	-0.194	0.191	0.247	0.321
54	-0.305	-0.244	-0.19	0.187	0.243	0.315
56	-0.299	-0.239	-0.186	0.184	0.238	0.309
58	-0.294	-0.234	-0.183	0.181	0.233	0.303
60	-0.289	-0.23	-0.179	0.177	0.229	0.297
62	-0.284	-0.226	-0.176	0.174	0.225	0.292
64	-0.279	-0.222	-0.173	0.171	0.221	0.287
66	-0.274	-0.218	-0.17	0.169	0.218	0.282
68	-0.27	-0.215	-0.167	0.166	0.214	0.278
70	-0.266	-0.211	-0.165	0.164	0.211	0.274

Table 11: Auxiliary variables for the confidence interval for σ_u

N	$\alpha_1 = 0.02$	$\alpha_1 = 0.05$	$\alpha_1 = 0.10$	$\alpha_2 = 0.90$	$\alpha_2 = 0.95$	$\alpha_2 = 0.98$
72	-0.262	-0.208	-0.162	0.161	0.208	0.269
74	-0.259	-0.205	-0.16	0.159	0.205	0.266
76	-0.255	-0.202	-0.158	0.157	0.202	0.262
78	-0.252	-0.199	-0.155	0.155	0.199	0.258
80	-0.248	-0.197	-0.153	0.153	0.197	0.255
85	-0.241	-0.19	-0.148	0.148	0.19	0.246
90	-0.234	-0.184	-0.144	0.143	0.185	0.239
95	-0.227	-0.179	-0.139	0.139	0.179	0.232
100	-0.221	-0.174	-0.136	0.136	0.175	0.226
110	-0.211	-0.165	-0.129	0.129	0.166	0.215
120	-0.202	-0.158	-0.123	0.123	0.159	0.205

Table 11: Auxiliary variables for the confidence interval for σ_u (cont'd.)

N	$\alpha_1 = 0.02$	$\alpha_1 = 0.05$	$\alpha_1 = 0.10$	$\alpha_2 = 0.90$	$\alpha_2 = 0.95$	$\alpha_2 = 0.98$
5	0.604	0.683	0.766	2.277	2.779	3.518
6	0.623	0.697	0.778	2.03	2.436	3.067
7	0.639	0.709	0.785	1.861	2.183	2.64
8	0.653	0.72	0.792	1.747	2.015	2.377
9	0.665	0.729	0.797	1.665	1.896	2.199
10	0.676	0.738	0.802	1.602	1.807	2.07
11	0.686	0.745	0.807	1.553	1.738	1.972
12	0.695	0.752	0.811	1.513	1.682	1.894
13	0.703	0.759	0.815	1.48	1.636	1.83
14	0.71	0.764	0.819	1.452	1.597	1.777
15	0.716	0.77	0.823	1.427	1.564	1.732
16	0.723	0.775	0.826	1.406	1.535	1.693
17	0.728	0.779	0.829	1.388	1.51	1.66
18	0.734	0.784	0.832	1.371	1.487	1.63
19	0.739	0.788	0.835	1.356	1.467	1.603
20	0.743	0.791	0.838	1.343	1.449	1.579
22	0.752	0.798	0.843	1.32	1.418	1.538
24	0.759	0.805	0.848	1.301	1.392	1.504
26	0.766	0.81	0.852	1.284	1.37	1.475
28	0.772	0.815	0.856	1.269	1.351	1.45
30	0.778	0.82	0.86	1.257	1.334	1.429
32	0.783	0.824	0.863	1.246	1.319	1.409
34	0.788	0.828	0.866	1.236	1.306	1.392
36	0.793	0.832	0.869	1.227	1.294	1.377
38	0.797	0.835	0.872	1.219	1.283	1.363
40	0.801	0.839	0.875	1.211	1.273	1.351

Table 12: Auxiliary variables for the confidence interval for *m*

N	$\alpha_1 = 0.02$	$\alpha_1 = 0.05$	$\alpha_1 = 0.10$	$\alpha_2 = 0.90$	$\alpha_2 = 0.95$	$\alpha_2 = 0.98$
42	0.804	0.842	0.877	1.204	1.265	1.339
44	0.808	0.845	0.88	1.198	1.256	1.329
46	0.811	0.847	0.882	1.192	1.249	1.319
48	0.814	0.85	0.884	1.187	1.242	1.31
50	0.817	0.852	0.886	1.182	1.235	1.301
52	0.82	0.854	0.888	1.177	1.229	1.294
54	0.822	0.857	0.89	1.173	1.224	1.286
56	0.825	0.859	0.891	1.169	1.218	1.28
58	0.827	0.861	0.893	1.165	1.213	1.273
60	0.83	0.863	0.894	1.162	1.208	1.267
62	0.832	0.864	0.896	1.158	1.204	1.262
64	0.834	0.866	0.897	1.155	1.2	1.256
66	0.836	0.868	0.899	1.152	1.196	1.251
68	0.838	0.869	0.9	1.149	1.192	1.246
70	0.84	0.871	0.901	1.146	1.188	1.242
72	0.841	0.872	0.903	1.144	1.185	1.237
74	0.843	0.874	0.904	1.141	1.182	1.233
76	0.845	0.875	0.905	1.139	1.179	1.229
78	0.846	0.876	0.906	1.136	1.176	1.225
80	0.848	0.878	0.907	1.134	1.173	1.222
85	0.852	0.881	0.91	1.129	1.166	1.213
90	0.855	0.883	0.912	1.124	1.16	1.206
95	0.858	0.886	0.914	1.12	1.155	1.199
100	0.861	0.888	0.916	1.116	1.15	1.192
110	0.866	0.893	0.92	1.11	1.141	1.181
120	0.871	0.897	0.923	1.104	1.133	1.171

Table 12: Auxiliary variables for the confidence interval for m (cont'd)

(r=1mm)	ML intervals		BC intervals		(r=2mm)	ML intervals		BC intervals	
Quantiles	m	σ_u	m	σ_u	Quantiles	m	σ_u	m	σ_u
0.02	7.4	1846.2	8.0	1863.9	0.02	6.8	1993.1	8.6	1765.4
0.05	8.2	1868.6	9.0	1831.0	0.05	7.5	2019.3	8.9	1787.4
0.10	9.0	1887.0	9.2	1796.1	0.10	8.3	2040.8	9.1	1802.0
0.90	15.5	2003.7	13.9	2183.5	0.90	14.3	2178.1	19.3	2242.7
0.95	16.6	2022.0	14.7	2115.5	0.95	15.3	2199.7	20.8	2282.7
0.98	17.8	2044.6	15.8	2183.5	0.98	16.5	2226.4	25.6	2307.9

Table 13: Maximum likelihood (ML) confidence intervals of -150° C results compared with bias-corrected (BC) bootstrap confidence intervals for F82Hmod.

(r=0.5mm)	ML intervals		BC intervals		(r=2mm)	ML intervals		BC intervals	
Quantiles	m	σ_u	m	σ_u	Quantiles	m	σ_u	m	σ_u
0.02	9.9	2160.1	9.6	2071.0	0.02	51.0	2195.2	54.0	2202.9
0.05	11.2	2181.5	11.2	2124.5	0.05	58.5	2199.5	60.7	2205.5
0.10	12.5	2199.2	11.4	2161.1	0.10	66.0	2203.0	62.7	2206.9
0.90	24.1	2306.2	22.5	2448.6	0.90	131.7	2223.6	126.9	2218.4
0.95	26.1	2323.5	24.9	2455.2	0.95	143.2	2226.9	149.6	2220.3
0.98	28.4	2346.4	28.9	2629.3	0.98	156.3	2231.4	174.3	2222.9

Table 14: Maximum likelihood (ML) confidence intervals of -150° C results compared with bias-corrected (BC) bootstrap confidence intervals for EUROFER97.